Beamforming Performance Evaluation with Impact of User Model Electric Properties

Ivan Lomillos Rozeboom, BSc Thesis
Faculty of Electrical Engineering, Mathematics and Computer Science
University of Twente

Abstract— **In this paper, the Maximal Ratio Combining (MRC) output from a Uniform Linear Array (ULA) antenna in the proximity of the human body is analyzed by means of numerical simulations. The idealized situation is considered where the far-field radiated by a base station or access point is assumed to be a vertically polarized plane wave impinging on an infinite homogeneous cylinder emulating the human body. The antenna elements of the ULA are idealized isotropic radiators with no coupling between each other. The total electric field due to the plane wave and the scattered field by the infinite homogeneous cylinder is computed using the well-known expansion of the electromagnetic field in cylindrical vector wave functions. In order to investigate the impact of the human body tissue on the MRC performance at different frequencies, two models of the equivalent dielectric material of the user have been considered. Results are compared to an infinite cylinder made of a perfect electric conductor (PEC) material. In the evaluation, two figures of merit have been considered: (i) the perceived MRC-gain and (ii) the real MRC-gain, where either the received power of the center element is used or the maximum power received by any of the elements is used, respectively. The simulations were performed at the frequencies 1, 30 and 60 GHz and for separation distances between the ULA and the cylinder equal to 10 and 20 cm. As a result of the presented investigations it is concluded that the two suggested approaches to compute the equivalent dielectric parameters of the homogeneous cylindrical model of the human body are rather similar. It is shown that a perfect electric conductor PEC is a good approximation of the human equivalent model for the considered scenarios.**

I. INTRODUCTION

Human kind is constantly putting more trust in the use of wireless communications to the point where these can be found everywhere. The trend for the past few decades has been to focus on the use of user-end devices, these becoming ever smaller and using higher frequencies and bandwidths. What half a century ago could only be achieved by a huge antenna on the top of a building has now been out-competed by smartphone devices found in virtually everybody's pocket.

What this entails is that humans are becoming the cornerstones of wireless communications and while the burden of cost and complexity still falls on the base stations of the service providers, it is predicted that the user equipment, i.e., smartphones, laptops, smartwatches, etc., might make use of beamforming technology too. It is for this reason that a thorough understanding of the interactions between users an antennas is needed.

Many studies of the interactions between humans and electromagnetic waves have been conducted to ensure safe guidelines and restrictions are placed for the use of wireless communications [1]-[3]. However, studies are not as readily available for the performance of antennas in the presence of human-model obstacles.

Many studies have been conducted to analyze the interactions between antenna and head like the one in [4] however, more generalized models of human obstacles are sparse.

It has been proven in [1] that the scattering of a human body can be approximated by that of an infinite cylinder of equivalent dielectric material. Based on that, a simulator is proposed that computes the scattered electric field of a 2D cross-section of an infinite cylinder. This scattered field is then probed at locations corresponding to a uniform linear array (ULA) antenna and the performance of said antenna is analyzed.

The implementation of a ULA antenna using maximal ratio combinig (MRC) is explained in Section II. In Section III the scattering problem by the cylinder is analyzed and solutions are given for both the dielectric and the perfect electric conductor (PEC) cases. A model is described in Section IV, where a widely used human model based on tissue thickness is described and an equivalent dielectric model is computed using a dielectric mixing method. The results of the simulation are presented and analyzed in Section V.

II. SYSTEM MODEL AND SIMULATION SCENARIO

In this section the simulation scenario and the system model are presented.

In Fig. 1, the toy model used in this paper can be seen, where the user is modelled as a homogeneous infinite cylinder of radius r. Furthermore, the user is assumed to be carrying a device equipped with a Uniform Linear Array (ULA) with N_{el} antenna elements separated by the distance $d_{\mathrm{el}} = \lambda/2$, where λ is the wavelength corresponding to the carrier frequency f of the transmitted signal. In Fig. 1 each dot represents the position of an antenna element in the ULA for $N_{\mathrm{el}} = 3$. The ULA is placed symmetrically and perpendicularly to the radius of the cylinder. The distance between the ULA and the cylinder is denoted by d_0. The signal source, e.g., a base station or a WiFi access point, is assumed to be located in the far-field from the user.

Furthermore, it is assumed that a monochromatic vertically polarized (the $\boldsymbol{E}$-field is oriented parallel to the z-axis) plane wave with angular frequency $\omega = 2\pi f$ and complex

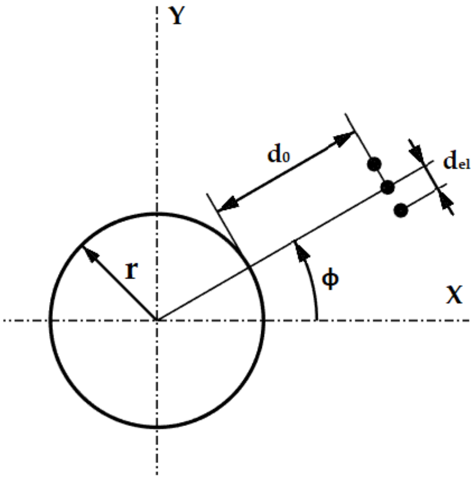

Fig. 1: Sketch showing the layout of the simulation experiment including all variables used

amplitude E_z^{i} is impinging at the cylinder. This plane wave will be scattered by the cylinder and the total field E_z outside the cylinder will be the sum of the incident plane wave field E_z^{i} and the scattered wave field E_z^{s}. For the sake of simplicity it is assumed in this paper that the antenna elements of the ULA are ideal isotropic antennas. It is further assumed that the coupling between this ideal antenna elements can be neglected. Hence, the voltage v_i induced at the port of an antenna element i is assumed to be proportional to the total electric field at the location where each element of the ULA should lay

$$v_i = E_z(\boldsymbol{r}_i), \tag{1}$$

where $\boldsymbol{r}_i$ is the radius vector indicating the position of (virtual) antenna element i. The equality sign in (1) has been used to simplify the computation without the loss of too much generality. It should be noted also, as shown further below, that since we are interested in power ratios the proportionality constants will cancel each other under the assumed idealized conditions.

1. Maximum Ratio Combining or Matched Filter Beamforming

In this section, an algorithm is selected to be used in order to combine the received signals at each one of the individual elements of the array.

The algorithms used to combine the received signals while maximizing performance measures are known as diversity combining techniques and most of them make use of a linear combination of the N_{el} received signals

$$v = \sum_{i=1}^{N_{\mathrm{el}}} w_i v_i, \tag{2}$$

where each one of the v_i represents the signal received at each one of the elements in the ULA and w_i represent the weights applied to each branch.

The problem at hand now is to find a set of suitable weights w_i to apply to each one of the received signals. The solution to this problem that will be implemented in the simulation is known as Maximal-Ratio Combining (MRC) and has been proven to maximize the received power (or the SNR in the presence of noise) for both correlated and uncorrelated branches or voltages v_i [5]-[7].

If the system is noiseless the instantaneous signal is measured and no Additive White Gaussian Noise (AWGN) is present, the weights that maximize (2) are the complex conjugate values of the excitation voltages

$$w_i = \frac{v_i^*}{\sqrt{\sum_{i=1}^{N_{el}} |v_i|^2}}, \tag{3}$$

where * indicates the complex conjugate operation. The normalization is the result of applying the unity norm condition for the combining, or in general, the beamforming, weights

$$\sum_{i=1}^{N_{el}} |w_i|^2 = 1, \tag{4}$$

Hence, the output voltage of the antenna (2) after the MRC-beamforming (3) becomes

$$v = \sqrt{\sum_{i=1}^{N_{el}} |v_i|^2}, \tag{5}$$

It is further assumed, for simplicity, that the receive power is equal to the squared voltage (5). Now using (1) the receive power after applying MRC weights can be computed as

$$P_{\mathrm{mrc}} = \sum_{i=1}^{N_{el}} |E_z(\boldsymbol{r}_i)|^2. \tag{6}$$

Hence, in this paper it is assumed that the received power is proportional to the intensity of the computed electric field at the position of each element of the ULA.

2. MRC-gain

The performance of the ULA using MRC is evaluated here as the MRC-gain

$$G_{\mathrm{mrc}}(\phi) = \frac{P_{\mathrm{mrc}}(\phi)}{P_{\mathrm{ref}}(\phi)}, \tag{7}$$

where $P_{\mathrm{mrc}}(\phi)$ is given by (6) and $P_{\mathrm{ref}}(\phi) = |E_z(\boldsymbol{r}_{\mathrm{ref}}(\phi))|^2$ is the power received by a single antenna element used as reference. The dependence on the rotation angle ϕ (see Fig. 1) has now been explicitly shown. In this study, the reference antenna is also an ideal isotropic radiator as assumed for the ULA.

The reference signal can be defined in different ways. For example, the reference signal can be taken to be the total electric field computed at the center of the ULA as shown in Fig. 1. However, as will be shown in Section V, defining the reference point at the center of the ULA can be deceiving and give disproportionate gains in some situations. For this reason a second measure is made by taking the antenna element with the maximum received intensity as the referenece.

Hence, two figures of merit for the MRC-gain are considered in this paper: (i) the MRC-gain where the reference is the antenna element located in center of the array, which is denominated as perceived MRC-gain and denoted as $G_{\text{mrc\_PERC.}}$, and (ii) the MRC-gain where the reference is the antenna element with the maximum received power, which is denominated as real MRC-gain and is denoted as $G_{\text{mrc\_REAL}}$.

III. SCATTERING BY A CYLINDER

This section presents the canonical solution of the 2D electromagnetic scattering of a plane wave by an infinite homogeneous cylinder to obtain the total field at any point outside the cylinder. Section III-1 shows the scattering by a perfect electric conductor (PEC) cylinder while Section III-2 does so for a homogeneous cylinder of dielectric material emulating the electrical properties of the human tissue. The computations are obtained using a modified version of the MATLAB-script in [8]. These results will then be used to obtain $E_z(\boldsymbol{r}_i)$ and $E_z(\boldsymbol{r}_{\text{ref}})$ explained above.

1. PEC Cylinder

A plane wave is propagating in the positive $x-$axis direction. The infinite cylinder is aligned with the $z-$axis of the coordinate frame. A schematic of the 2D cross-section representing the simulation scenario can be found in Fig. 2. This figure also shows the Cartesian and cylindrical coordinate frames used.

Since the boundary problems that need to be solved coincide with the surface of a cylinder, the problem gets simplified if cylindrical coordinates are used. The interaction between an incident plane electromagnetic wave and a PEC cylinder is an ample studied scattering problem for which exact solutions exist. The total field outside the cylinder can be expressed as the sum of the incident wave and the scattered field as in equation (8) [9].

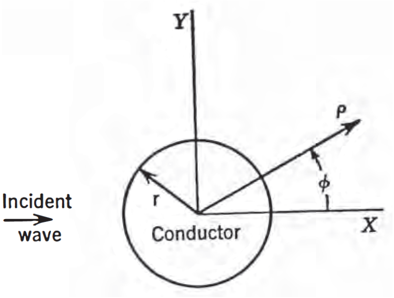

Fig. 2: Schematic showing the layout of the scattering problem [9].

$$E_z = E_z^i + E_z^s. \tag{8}$$

The subscript z denotes transverse polarization in the z direction while i and s denote incident and scattered field respectively.

Since a plane wave is considered, the incident electric field of a z-polarized wave propagating in positive x can be expressed as in equation (9).

$$E_z^i = E_0 e^{-jkx} = E_0 e^{-jk\rho\cos\phi}, \tag{9}$$

where k is the wave number. The middle term represents the wave using Cartesian coordinates while the right-term uses cylindrical coordinates. The incident field of equation (9) can be expressed in terms of cylindrical waves as

$$E_z^i = E_0 \sum_{n=-\infty}^{\infty} j^{-n} J_n(k\rho) e^{jn\phi}, \tag{10}$$

where J_n is the Bessel function of the first kind. To represent the scattered field component of the electric wave, the equation for an outward travelling wave needs to be used. This is found in equation (11)

$$E_z^s = E_0 \sum_{n=-\infty}^{\infty} j^{-n} a_n H_n^{(2)}(k\rho) e^{jn\phi}, \tag{11}$$

where $H_n^{(2)}$ represents the Bessel function of the fourth kind, more commonly referred to as Hankel function of the second kind.

Substituting equations (10) and (11) into equation (8), the total field can be expressed as

$$E_z = E_0 \sum_{n=-\infty}^{\infty} j^{-n} [J_n(k\rho) + a_n H_n^{(2)}(k\rho)] e^{jn\phi}. \tag{12}$$

The last step to follow in order to arrive to a solution for the scattering problem of a PEC cylinder is to solve the boundary condition at the edge of the cylinder. In this case, this is straightforward. Since the electric field inside a PEC material is always zero, the electric field at the boundary needs to be zero as well, i.e., the condition $E_z = 0$ at $\rho = r$ must be met [9].

It is clear from looking at equation (12) that the condition holds true for the values of a_n such that

$$a_n = -\frac{J_n(kr)}{H_n^{(2)}(kr)}. \tag{13}$$

The field outside the PEC cylinder is then given by inserting (13) into (12).

2. Dielectric Cylinder

The solution for the problem of a plane wave scattered by an infinite cylinder of dielectric material is more complicated. The incident electric field and scattered field are still described by equations (10) and (11) respectively. However, in this case the field inside the cylinder is not zero. The transmitted field E_z^t, i.e. the field inside the cylinder, can be described by

$$E_z^t = E_0 \sum_{n=-\infty}^{\infty} [b_n J_n(k_1\rho) + c_n Y_n(k_1\rho)] e^{jn\phi}, \tag{14}$$

where Y_n is the Bessel function of the second kind and k_1 is the wave number inside the cylinder. To solve the problem, the boundary conditions at the surface of the cylinder have to be considered to find a_n, b_n and c_n. The boundary conditions need the tangential components of the electric field to be continuous at the surface of the cylinder [10]. This can be expressed according to equations

$$(E_z^i + E_z^s - E_z^t) \times \hat{\rho} = 0 \quad \text{for} \quad \rho = r, \tag{15}$$

$$[\nabla \times (E_z^i + E_z^s - E_z^t)] \times \hat{\rho} = 0 \quad \text{for} \quad \rho = r, \tag{16}$$

where (10), (11) and (14) are employed. The full derivation of the three unknowns will not be given here as it goes beyond the scope of the paper and it can be found in sources like [11]. The values of a_n, b_n and c_n obtained are:

$$a_n = j^{-n} \frac{J_n'(kr)J_n(k_1r) - \sqrt{\frac{\varepsilon}{\mu}} J_n(kr)J_n'(k_1r)}{\sqrt{\frac{\varepsilon}{\mu}} J_n'(k_1r)H_n^{(2)}(kr) - J_n(k_1r)H_n^{(2)}{}'(kr)}, \tag{17}$$

$$b_n = j^{-n} \frac{J_n(kr)H_n^{(2)}{}'(kr) - J_n'(kr)H_n^{(2)}(kr)}{J_n(k_1r)H_n^{(2)}{}'(kr) - \sqrt{\frac{\varepsilon}{\mu}} J_n'(k_1r)H_n^{(2)}(kr)}, \tag{18}$$

$$c_n = 0, \tag{19}$$

where J_n' is the derivative of Bessel's function of the first kind and $H_n^{(2)}{}'$ is the derivative of Hankel's function of the second kind. Moreover, k is the wave number computed in free space while k_1 is the wave number computed inside the cylinder. Since in the simulations the electric field inside the cylinder is not needed, only the a_n factor will have to be implemented.

3. Infinite series truncation

One last consideration needs to be made for the computing of the scattered field, for both the PEC and dielectric cylinder solutions. The total field outside the cylinder as described by equation (14) is obtained after a summation of an infinite number of Bessel's and Hankel's functions orders. This, in practice, is not feasible so a compromise needs to be made. The number of orders to be computed needs to remain high enough so that the computed electric field closely approximates the real case while achieving a relatively high computation speed. For this reason, the maximum order of functions to compute is decided with a method based on that proposed by [12].

$$N = \begin{cases} x + 4x^{1/3} + 1, & 0.02 \leq x \leq 8 \\ x + 4.05x^{1/3} + 2, & 8 < x < 4200, \\ x + 4x^{1/3} + 2, & 4200 \leq x \leq 20000 \end{cases} \tag{20}$$

where N is the maximum mode order used in the computations and x is the circumference of the cylinder r divided by the wavelength or rather $x = kr$, where k is the wave number. It can be seen from equation (17) that the scattered field by a dielectric cylinder depends on the dielectric properties of the cylinder.

In the next section, the process followed to obtain said properties for a human-model dielectric cylinder is explained.

IV. CYLINDER MODEL OF HUMAN BODY

It has already been stated that an infinite cylinder of dielectric material will be used in the simulation to approximate the human body. In sections IV-1 and IV-2, the main theory behind the dielectric properties of human tissue and the specific values used for the simulations are explained respectively.

1. Dielectric Model of Human Tissue

The dielectric properties of human tissue are frequency dependent and are usually presented as a complex relative permittivity ε^*

$$\varepsilon^*(\omega) = \varepsilon' - j\varepsilon'' \tag{21}$$

where ε' is the relative permittivity of the material and ε'' is the frequency dependent out-of-phase loss factor associated with power dissipation in the material defined as:

$$\varepsilon'' = \frac{\sigma}{\omega\varepsilon_0}, \tag{22}$$

where $\sigma[S \cdot m^{-1}]$ is the conductivity of the material, $\omega[rad \cdot s^{-1}]$ is the angular frequency of the electromagnetic wave and $\varepsilon_0 = 8.85 \cdot 10^{-12}[F \cdot m^{-1}]$ is the permittivity of free space [13].

Both the relative permittivity and conductivity of human tissues are frequency dependent. The relative permittivity slowly decreases with increasing frequency while the conductivity increases. At certain frequencies, these parameters decrease or increase in big steps due to relaxation phenomena. For the frequency range of the simulations, the γ relaxation (in the low GHz region) is of great importance [13]. This relaxation is caused by the polarization of water molecules and happens at a frequency of 20 GHz for free water. Different tissues contain different amounts of water, which translates to different frequency dependent complex relative permittivity. More important is the content of free and bound water, which causes the relaxation frequency to shift to lower frequencies. In order to capture and describe the dielectric properties of human tissues at frequencies around said relaxation frequency, the Debye equation or the more general Cole-Cole equation can be used. The one-term Cole-Cole equation is

$$\varepsilon^* = \varepsilon_\infty + \frac{\Delta\varepsilon}{1 + (j\omega\tau)^{1-\alpha}} + \frac{\sigma}{j\omega\varepsilon_0}, \tag{23}$$

where $j = \sqrt{-1}$, ω is the angular frequency, $\tau[s]$ is the relaxation time of the dispersion mechanism and ε_∞ is the permittivity at frequencies where $\omega\tau >> 1$. Furthermore, $\Delta\varepsilon = \varepsilon_s - \varepsilon_\infty$ with ε_s being the permittivity at frequencies where $\omega\tau << 1$, α is used to account for the spread in relaxation time and σ_s is the static ionic conductivity [2]. The Debye equation is a simplification of (23) that arises when $\alpha = 0$.

Many studies about the dielectric properties of tissues have been conducted in the past century mainly motivated to find accurate information to establish dosimetric restrictions in the use of electromagnetic radiation. Of particular importance are those of Gabriel *et al.* [13]-[15] which made a vast analysis of the available literature, made measurements showing accordance with the analysis and provided the best fitting curves in the form of four-term Cole-Cole equation defined as

$$\varepsilon^* = \varepsilon_\infty + \sum_{n=1}^{4} \frac{\Delta\varepsilon_n}{1+(j\omega\tau_n)^{1-\alpha}} + \frac{\sigma}{j\omega\varepsilon_0} \tag{24}$$

As can be seen from equations (23) and (24) the name one-term Cole-Cole as opposed to the name four-term Cole-Cole describe the number of terms used in the summation of the middle element in equation (24). Each one of this terms is used to describe one of the frequency dispersions. There are three of these dispersions in the frequency range from 1 Hz to 100GHz. The reason for Gabriel *et al.* [13]-[15] to heve four terms is to provide a better adjustment to the measured data by adding an extra term.

Although one or two term equations would suffice for the frequency range being simulated, the descriptions provided in [15] in the form of four-term Cole-Cole equations will be used to compute the dielectric parameters at the desired frequencies. The reason to do so is that many scientific papers make use of them and have shown accordance with these descriptions [3].

2. *Model of Effective Dielectric Cylindrical Human Model*

In the present paper the human body is modeled by an homogeneous infinite cylinder. However, the human body is composed of an enormous amount of different tissues, each with its corresponding dielectric parameters represented by equation (24). Therefore, an effective dielectric model based on a composite-dielectric infinite cylinder will be used. The first step to do so is to identify the tissues that make up the composite dielectric and the proportion of the cross-section that they occupy. To do so, a widely used model based on mean values for three levels of visceral fat, muscle and subcutaneous fat thickness in women's waist will be used[16]-[18].

Said model provides maximum and minimum thicknesses of human skin, subcutaneous fat, abdominal muscle, and visceral fat. The value of thickness used will be the average between maximum and minimum values. It also provides average waist circumference measurements for the three levels. After substracting the thicknesses of the mentioned tissues from the total one obtained from the circumference, the proportion occupied by other organs can be calculated. Since the cross-section taken is obtained from the waist, the dielectric material for the remaining organ section will be assumed to be made of small intestine tissue. The tissues selected for each layer alongside their thickness ranges are shown in Table I.

TABLE I: Abdomen tissue thickness (mm) [19]-[21]

		Type 1	Type 2	Type 3
1	**Small Intestine (SI)**	52	52	52
2	**Visceral Fat**	15-36	37-47	47-98
3	**Muscle**	8-16	8-16	8-16
4	**Subcutaneous Fat**	17-34	17-34	20-33
5	**Skin**	1.1-1.6	1.1-1.6	1.1-1.6

The reason for selecting only women is that the differences between the three visceral fat levels is evenly spaced. In the case of men, there is a very big gap between levels 2 and 3 with levels 1 and 2 mostly overlaping with women.

To get the cylinder radii for each of the three cylinders, the average between the maximum and minimum thickness of each layer in Table I is taken. After summing the averages obtained for each layer, a radius for each one of the three types is obtained. The values obtained are therefore $r_1 = 11.6$ cm, $r_2 = 13.3$ cm and $r_1 = 16.4$ cm corresponding to the cylinders of Type 1, Type 2 and Type 3 respectively. A schematic representation of the layered cylinders obtained from the thicknesses listed in Table I is shown in Fig. 3. The values obtained from this model will be used to calculate the proportion of the cross-section area that each one of the tissues will occupy. The proportions calculated are shown in Table II

TABLE II: Fraction of total volume per tissue

	Type 1	Type 2	Type 3
Small Intestine (SI)	19.97%	15.32%	10.01%
Fat	62.91%	69.06%	76.76%
Muscle	14.80%	13.60%	11.60%
Skin	2.32%	2.02%	1.63%

Note that the subcutaneous and visceral fat tissues are considered together. The reason for this will be explained shortly.

Now that the proportions of each one of the tissues have been obtained, the dielectric properties of each one of the tissues needs to be assigned. The dielectric parameters of the tissues are taken from [15], which describes them as four-term Cole-Cole equations. The skin is composed by a submillimiter outer dry layer (epidermis) and an inner layer (dermis) inflitrated with blood vessels. Since this second layer takes up most of the skin thickness, it will be assumed that all the skin is composed by the infiltrated tissue (wet skin). Similarly, there are two types of fat listed in [15], infiltrated and non infiltrated describing the different amounts of blood vessels in the tissue. Since almost all of the visceral fat and a great deal of the subcutaneous layer are highly infiltrated [22], the infiltrated model will be used for all the fat. Finally, there is no model included in [15] for the small intestine. For this reason, the values for different frequencies are obtained from [23] and a two term Cole-Cole equation is fitted to the curve.

A table showing the parameters for each one of the four-term Cole-Cole equations obtained from [15] as well as the self-derived two-term one for the small intestine are shown in Table III.

Lastly, since the homogeneous cylinder model of the human body is being applied, it is convenient to compute an effective complex permittivity that accounts for the stratified nature of the cylinder. To do so, the proportions of the cross-section or volume listed in Tables I and II need to be

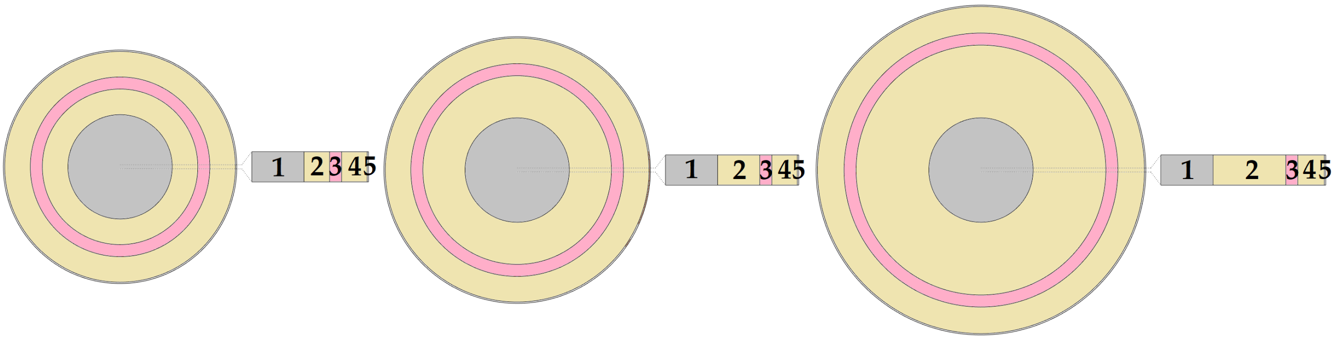

Fig. 3: Schematic of the layered cylinders obtained from the averaged thickness of each tissue liste in Table I. The leftmost cylinder represents a Type 1 cylinder, the center one a Type 2 ant the rghtmost one represents a Type 3 cylinder.showing the averaged thicknesses of the different tissues in the Type 2 model of Table I.

TABLE III: Parameters of 4-term Cole-Cole expansions. Gabriel *et al.* [13]-[15]

	ε_∞	$\Delta\varepsilon_1$	$\tau_1[ps]$	α_1	$\Delta\varepsilon_2$	$\tau_2[ns]$	α_2	$\Delta\varepsilon_3$	$\tau_3[\mu s]$	α_3	$\Delta\varepsilon_4$	$\tau_4[ms]$	α_4	σ_i
Skin (wet)	4.0	39	7.96	0.1	280	79.58	0.0	$3.0 \cdot 10^4$	1.59	0.16	$3.0 \cdot 10^4$	1.592	0.20	0.0004
Fat (infiltrated)	2.5	9	7.96	0.2	35	15.92	0.1	$3.3 \cdot 10^4$	159.15	0.05	$1.0 \cdot 10^7$	15.915	0.01	0.0350
Muscle	4.0	50	7.23	0.1	7000	353.68	0.1	$1.2 \cdot 10^6$	318.31	0.10	$2.5 \cdot 10^7$	2.274	0.00	0.2000
Small Intestine	4.0	50	7.96	0.1	0	–	–	$1.2 \cdot 10^6$	16.90	0.10	0	–	–	0.2000

combined with the dielectric properties of each layer listed in Table III.

This will be done in two ways. The first one, and simplest, will just be a weighted average of the dielectric properties of each layer. The proportion of the cylinder volume obtained from the concentric cylinder model seen in Fig. 3 and listed in Table II for each layer is multiplied by the dielectric properties of said layer at the given frequency as listed in Table III. The values for each layer are then added to obtain the dielectric properties of the homogeneous cylinder.

The second method will try to take into account the geometry of the different tissues included in the model. To look at a real cross-section of a human waist, an MRI scanner showing the axial cross-section of an abdomen can be seen in Appendix I. Said image has been obtained from an online resource providing many more cross sections [24]

It has been proven by [25] that due to the granular nature of tissues and their heterogeneous distribution, the homogeneous dielectric model of a human body is better approximated by a mixture of a host material of dielectric constant ε_h, i.e the predominant material, with granular inclusions of dielectric constants ε_i . These inclusions are randomly distributed through the body and can be of different sizes. This seems to be in accordance with the MRI scanner of a human abdomen seen in Appendix I.

A method proposed by de Loor [26] is used to compute the equivalent or effective complex permittivity of the cylinder described by the following equation:

$$\varepsilon_{\text{eff}} = \varepsilon_h + \sum_{i=1}^{N} \frac{V_i}{3}(\varepsilon_i - \varepsilon_h) \sum_{j=1}^{3} \frac{1}{1 + (A_j(\frac{\varepsilon_i}{\varepsilon^*}) - 1)}, \qquad (25)$$

The last step is to find the appropiate parameters to fill in in equation (25). Variables ε_h and ε_i have already been stated to be the host and inclusion permittivity respectively. Since fat takes up most of the cross-section volume proportion, it will be used as the host material. All other tissues will, therfore, be inclusions. V_i represents the volume fraction of inclusion i with respect to the host tissue volume. It can therefore be calculated as the ratio between inclusion and host material proportions as taken from Table II. For example, the V_{iSKIN} for the cylinder of Type 1 is calculated as: $V_{i\text{SKIN}} = \frac{2.32}{62.91} \cdot 100 = 3.67\%$. All the V_i calculated for the tissues at the three given thicknesses can be found in Table IV.

The parameter ε^* is the effective permittivity of the material surrounding the inclusion. This will depend on the volume fraction of each of the inclusions being considered. If V_i is less than 10%, it is assumed that it is fully surrounded by host material and therefore ε^* can be assumed to be equal to the host permittivity ε_h. If it is bigger, it is assumed that the inclusion is surrounded by both host material and inclusion and ε^* becomes ε_{eff}. Finally, A_j depends on the geometry of the inclusions. For simplicity, it will be assumed that these inclusions are spherical. This has been shown to be the best approximation for randomly shaped organs and tissues inside a human body. Therefore, the values of A_j are $A_1 = A_2 = A_3 = \frac{1}{3}$ [25].

TABLE IV: Fraction of host material volume per tissue

	Type 1	**Type 2**	**Type 3**
$V_{i\text{MUSCLE}}$	23.53%	19.69%	15.11%
$V_{i\text{SI}}$	31.75%	22.19%	13.04%
$V_{i\text{SKIN}}$	3.67%	2.93%	2.13%

So far, two methods have been described to calculate the equivalent dielectric properties of a composite dielectric material. The proportions listed in Table II have been used in both methods. Since the tissue proportions vary across the three different thickness types, this will result in different dielectric properties for each one of the cylinders. There will also be variations depending on the method used to combine the properties of the tissues.

To ilustrate this variability, the relative permittivity and conductivity of the different tissues of the layered cylinder along with the computed equivalent permittivity and conductivity are shown in Fig. 12 for the frequency range from 1GHz to 60GHz. The equivalent dielectric properties obtained from the first method are labelled "Avg." while the ones obtained from he second method as described by equation (25) are labelled as "Eff.".

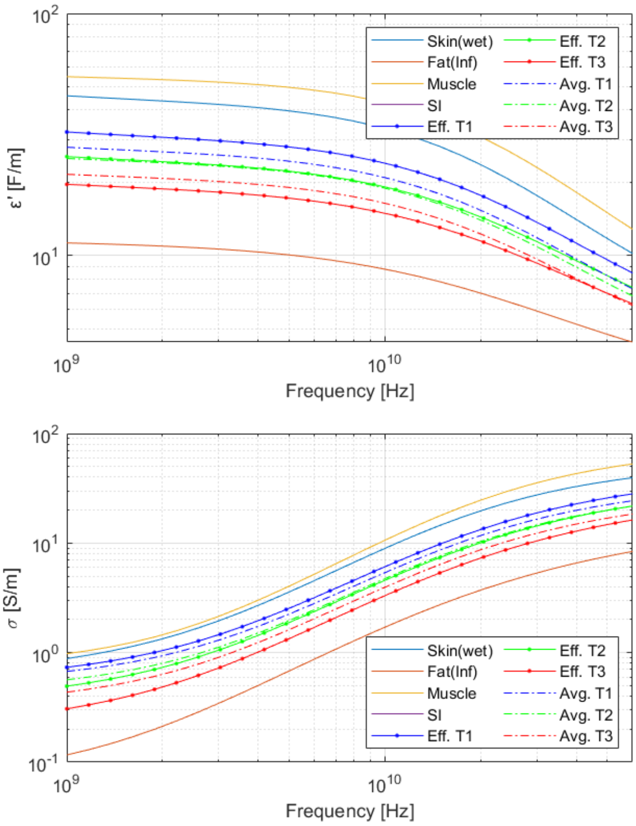

Fig. 4: Frequency dependent relative permittivity of different human tissues along with the equivalent relative permittivity and conductivity used to model the user cylinder.

As expected, the equivalent relative permittivity and conductivity falls between the bounds set by the permittivity and conductivity of the tissues composing the human model. Morover, the variations between the two methods used to calculate the effective permittivity are very small, especially for the Type 2 cylinder.

In order to better compare the results obtained using the Avg. and Eff. methods, the specific values of relative permittivity (ε') and conductivity (σ) obtained for each one of the three cylinders are listed in Table V. The values obtained for frequencies of 1, 30 and 60 GHz are listed as these are the frequencies being used in the simulations.

TABLE V: Values of ε' and σ obtained using the two different equivalent dielectric methods.

Radius	**Method**	**1GHz**		**30GHz**		**60GHz**	
		ε'	σ	ε'	σ	ε'	σ
Type 1	**Avg.**	32.41	0.73	13.75	18.85	8.49	28.17
	Eff.	28.03	0.67	11.88	16.53	7.30	24.37
Type 2	**Avg.**	25.64	0.49	11.44	14.34	7.39	21.82
	Eff.	25.20	0.56	10.91	14.65	6.83	21.73
Type 3	**Avg.**	19.71	0.31	9.32	10.47	6.34	16.27
	Eff.	21.67	0.44	9.68	12.31	6.23	18.41

It can be seen from the values listed in Table V that the differences between the two methods used to calculate the equivalent dielectric properties of the homogeneous material are small. The absolute differences in relative permittivity are reduced as the frequency increases while the absolute difference in conductivity increases with frequency.

Due to the variable nature of tissues, which are age, gender and location dependent [22], and the different measuring methods used, the dielectric values reported in literature show big differences [1], [28]-[30]. The differences obtained here between the Avg. and Eff. methods are well below those obtained in literature. In some cases, even below the difference between the values obtained using diffrent measurement methods on the same tissue sample. Therefore, it will be considered that the two methods used to obtain the equivalent dielectric properties are equivalent under the given conditions and the Eff. method will be used for the simulations.

V. SIMULATION RESULTS AND ANALYSIS

After the working principles behind the different parts comprising the simulator have been explained some of the most significant results are shown and analyzed to draw the relations between the parameters varied in the simulation and the performance of the ULA antenna. As a reminder, the parameters varied in the simulation are the frequency of the incident planar wave, the radius of the cylinder, the number of elements in the receiver array and the distance between the cylinder and the receiver. A list of the varied parameters alongside the range of values used in the simulations can be found on Table VI. In the following sections, the influence of every individual parameter is analyzed.

TABLE VI: Parameters varied in the simulation

Parameters	**Range**
Frequency (f)	1, 30 and 60 GHz
Angle (ϕ)	1, 2, ..., 360 degrees
Radius (r)	11.6, 13.3 and 16.4 cm
Distance (d_0)	10, 20 cm
N_{el}	1, 2, ..., 10

First, to have a better understanding of how the incident wave interacts with the cylinder, the absolute value of the total field (incident plus scattered) as a function of the x and y coordinates is plotted in Fig. 5. In order to better see the interactions on the part shaded by the cylinder, a logarithmic scale is used for the absolute values.

As can be seen from Fig. 5 barely any difference can be appreciated between the scattered field by a dielectric and PEC cylinders. However, there are a few things worth noting.

First, the total field shows a sinusoidal pattern with $\frac{\lambda}{2}$ distance between maxima and minima. This is caused by the interference between the incident wave, travelling in positive x direction, and the scattered field, travelling from the surface of the cylinder outwards.

Second, there is a big difference between the dielectric and PEC solutions regarding the field inside the cylinder. As was mentioned previously, the field inside the PEC cylinder is zero. In contrast, the field inside the dielectric cylinder is not. This is clearly the case for a 1GHz incident wave as can be seen in Fig. 5 a). However, at higher frequencies, i.e. for the 30GHz and 60GHz as seen in Fig. 5 b) and c), the transmitted field is attenuated under the -60dB level after a very short travel distance inside the cylinder. The signal is attenuated after a shorter distance for the higher frequency case. More precisely, for the 30GHz case in Fig. 5 b) the absolute value of the total field reaches -20dB after penetrating 1.8mm below the surface and -60dB after 8.3mm. In the case of the 60GHz wave of Fig. 5 c), the -20dB mark is reached after 1mm while the -60dB is reached after 4.5mm. This is a first indication that the dielectric model used is valid as several sources report only 1% [29] to 0.1% [14][1] of incident power penetrating further than the skin which can be up to 2.6mm wide depending on the location [22].

Finally, the differences between the calculated total fields when looking at the area behind the cylinder are big. In the case of the 1GHz incident wave of Fig. 5 a) and d), the shade created behind the cylinder barely reaches -30dB in the immediate vecinity of the cylinder and a relatively strong signal can be perceived after that. Since a 1GHz corresponds to a wavelength of $\lambda = 30$cm, and the diameter of the cylinder is 26.6cm in this case, the wavelength is greater than the obstacle and he electromagnetic wave will easily difract around the obstacle. When the frequency increases to 30Ghz as in Fig. 5 b) and e) or 60GHz as in Fig. 5 c) and f), the wavelengths become 1cm and 5mm respectively. In these cases, the wavelengths are much smaller than the size of the cylinder and the incident EM wave will bend much less around the edges of the cylinder. This can be seen in the figures as a shaded area behind the cylinder. This area is greater in the case of the 60GHz incident wave. This is known as blocking and is a major problem for mmWave 5G and higher frequency wireless systems that needs to be overcome. Nontheless, the wave bends around the cylinder to some extent as can be seen by the interference pattern created behind the cylinder.

All these observations were expected and show accordance with literature.

After this, the different simulations based on the different combinations of the parameters listed in Table VI are executed. The results are presented as polar plots of the gain of the maximal ratio combining algorithm as a function of the angle of the antenna. The simulations are performed for both $G_{\text{mrc\_PERC.}}$ and $G_{\text{mrc\_REAL}}$ for the dielectric and PEC cylinders. Since there are many graphs obtained from these simulations and the differences between the graphs are barely noticable to the naked eye, only a representative selection will be shown here and the rest of the plots will be shown in Appendix II.

Two figures are created to show the selected results. In these figures, only the intermediate size cylinder is used, i.e., the Type 2 cylinder corresponding to a radius of 13.3cm. Moreover, only the results obtained for a distance between cylinder and antenna $d_0 = 10$cm are shown.

In the first figure, seen in Fig. 6, the results obtained for $G_{\text{mrc\_PERC.}}$ are shown, i.e. the antenna element taken as a reference is the center element of the ULA array. The plots of the top row (Fig. 6 a), b) and c)) represent the results obtained for the dielectric equivalent model. The plots in the middle row (Fig. 6 d), e) and f)) are the equivalent simulations to those in the row above but with a PEC cylinder. Furthermore, the plots shown in the left-most column (Fig. 6 a), d) and g)) are those using a 1GHz plane wave. Those in the middle column (Fig. 6 b), e) and h)) use a frequency of 30GHz while those in the third (Fig. 6 c), f) and i)) use one of 60GHz. Lastly, the plots in the bottom row (Fig. 6 g), h) and i)) are a measure of the difference between the dielectric and PEC solution for every angle ϕ. The absolute difference is calculated as in equation (26) and is shown in logarithmic scale (dB)

$$\Delta G(\phi) = |G_{\text{PEC}}(\phi) - G_{\text{DIE}}(\phi)|, \tag{26}$$

where G_{PEC} and G_{DIE} are the MRC-gain computed for the PEC and the dielectric cylinders, respectively. In the case of Fig. 6, the gain used in equation (26) is $G_{\text{mrc\_PERC.}}$.

In the second figure, seen in Fig. 7, the same layout as is seen in Fig. 6 is followed but using the definition of gain $G_{\text{mrc\_REAL}}$ that uses the element with the maximum received intensity as its reference. The top row (Fig. 7 a), b) and c)) plots the results of the dielectric simulation. The middle row (Fig. 7 d), e) and f)) does so for a PEC cylinder. The bottom row (Fig. 7 g), h) and i)) shows the difference between the dielectric and PEC solutions as defined in equation (26). The left-most column (Fig. 7 a), d) and g)) shows the simulations for a 1GHz incident wave, the middle column (Fig. 7 b), e) and h)) for a 30GHZ wave while the right-most column (Fig. 6 c), f) and i)) does so for a 60GHz one.

It was already stated that the plots obtained for the dielectric and PEC cylinders that are not shown in the representative selection of Fig. 6 and Fig. 7 are shown in Appendix II. The results of calculating the difference ΔG between the dielectric and PEC cylindes as described in equation 26 are shown in Appendix III.

When looking at the polar plots shown in Fig. 6, it can be seen that the dielectric and perfect electric conductor solutions show very similar patterns. However, there are some important differences worth noting.

Out of all three frequencies being simulated, the 1GHz simulation seems to produce the most similar plots for the di-

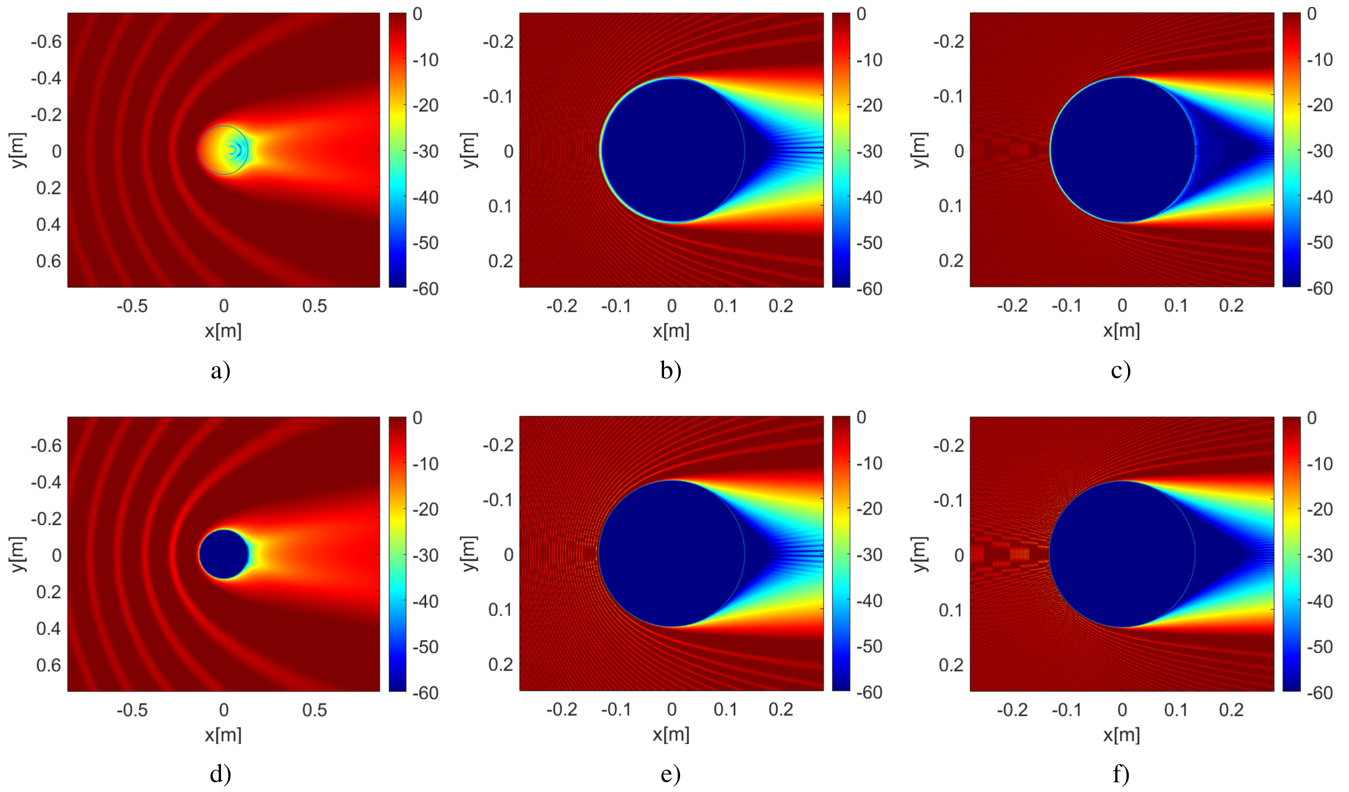

a) b) c)

d) e) f)

Fig. 5: Absolute value of the total electric field by a cylinder with 13.3cm (Type 2) radius as a function of position for an incident plane wave. Data is shown using a logarithmic scale (dB). In figure a), the cylinder is made of dielectric material for an incident wave of 1GHz. b) and c) use the same cylinder but for waves of 30GHz and 60GHz respectively. Figures d), e) and f) show the same situation as a), b) and c) respectively but for a PEC cylinder.

electric (Fig. 6 a)) and PEC (Fig. 6 d)) simulations. To better analyze the difference between them, the $\Delta G_{\mathrm{mrc\_PERC.}}$ of Fig. 6 g) needs to be looked at. In the case of the two-element antenna, the difference is below 0dB at all angles. In contrast, for the cases of 4 and 8 element antennas the difference between the two is only under 0dB in the region from 90 to 270 degrees, i.e. in the side of the incident wave. However, in the region hidden behind the cylinder the difference becomes positive. In the region roughly between 30 and -30 degrees, the difference reaches its maximum values which is of around 17dB for the 4 element antenna and 22dB for the 8 element case.

At first glance, the existance of these big ΔG seems at odds with the fact that the differences between dielectric Fig. 6 a) and PEC (Fig. 6 d) simulatons are very little. However, when looking at these more closely, some differences can be found explaining these ΔG. In the case of the 4 element antenna, the gain in the backwards direction reaches maximum values of 20dB for the dielectric cylinder and maximum values of around 22dB for the PEC cylinder. For the 8 element antenna, maximum gains of approximately 26dB and 28dB are reached. Since the difference ΔG is calculated in linear scale and then converted to dB, the differences that are barely noticeable between Fig. 6 a) and Fig. 6 d) result in values of 17dB for the 4 element antenna and 22dB for the 8 element case.

Furthermore, it can seem counterintuitive that such gain values are reached around the 0 degree angle, since this is the area where the cylinder is blocking the signal. The reason for this that the center element of the array, used as a reference at this point, will be the element receiving the lowest power. Furthermore, it was stated before that the inter-element distance d_{el} is half the wavelength of the incident wave. This means that the size of the antenna is frequency dependent. For the case of the 1GHz simulation, the wavelength is 30cm. Therefore, the 2 element antenna will be 15cm in size and will be fully blocked behind the cylider. This explains why the 2 element antenna has such a low gain around the 0 degree angle. In contrast, for the 4 and 8 element antennas, the sizes will be of 45 and 105 cm respectively. These sizes are greater than the diameter of the cylinder meaning that only a part of the antenna will be affected by the cylinder blocking while some part will receive direct line of sight transmision with the emmiting source.

A big difference can be appreciated between the simulation scenarios where the "low frequency" of 1GHz is used in contrast with those where "higher frequencies" of 30 and 60 GHz are used. This can be explained by the gaps in wavelenght, and hence in antenna sizes, between them. When going from a frequency of 1GHz to one of 30GHz, the inter element distance d_{el} of the antenna is reduced from 15cm

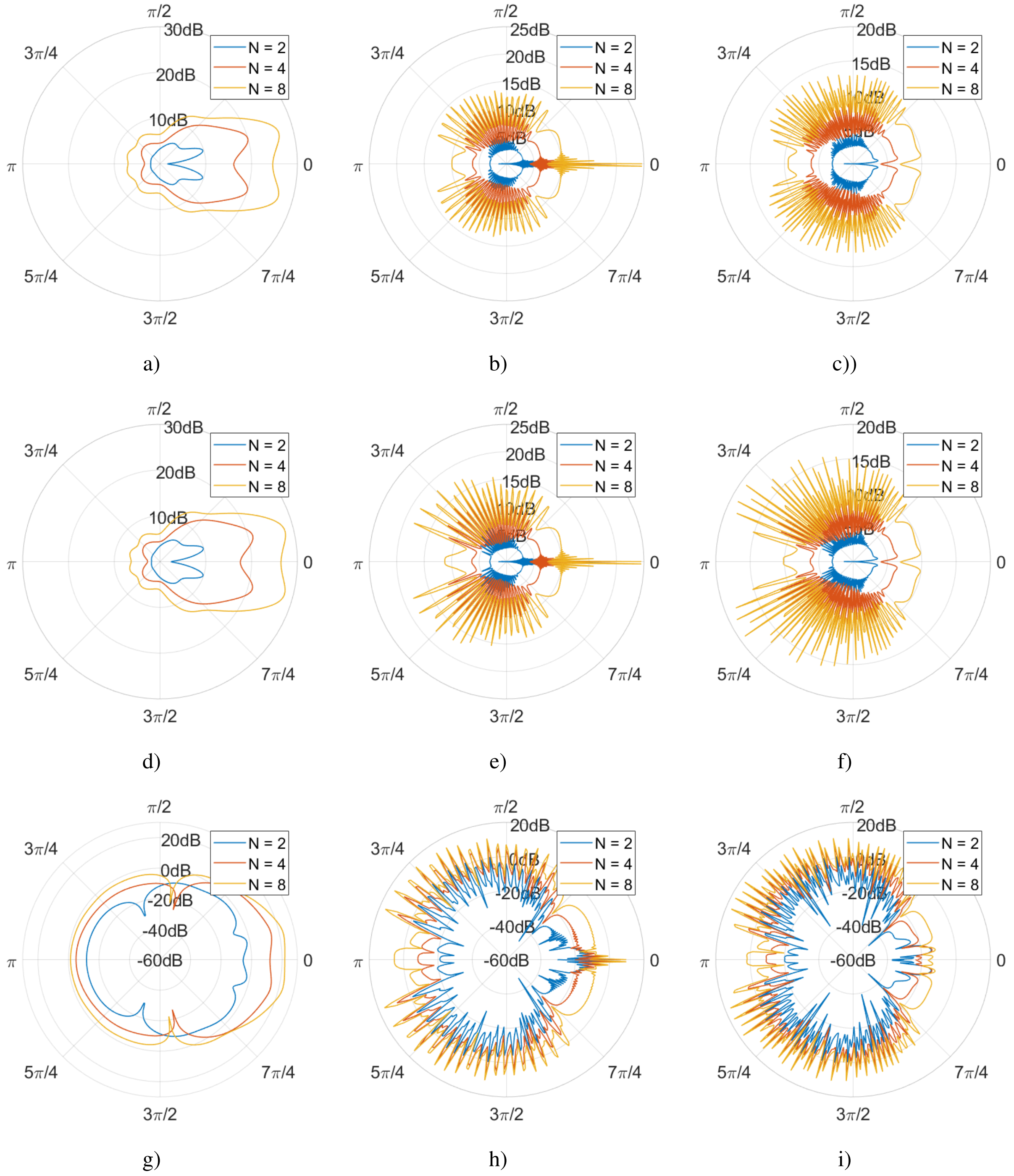

Fig. 6: $G_{\text{mrc\_PERC.}}$ as a function of the angle for an antenna located 10 cm away from the user model. The simulations for a plane wave of various frequencies impinging on a dielectric cylinder of 13.3 cm radius are shown. The leftmost column represents the simulations obtained for an incident wave of 1GHz. The centre column does so for a 30GHz wave while the right one depicts the 60GHz wave. The first row uses the dielectric model of the human cylinder while the second row uses a PEC one. The third row is the difference between the dielectric and PEC cylinders calculated using equation 26. Each tile depicts the gain of the antenna for 2, 4 and 8 elements.

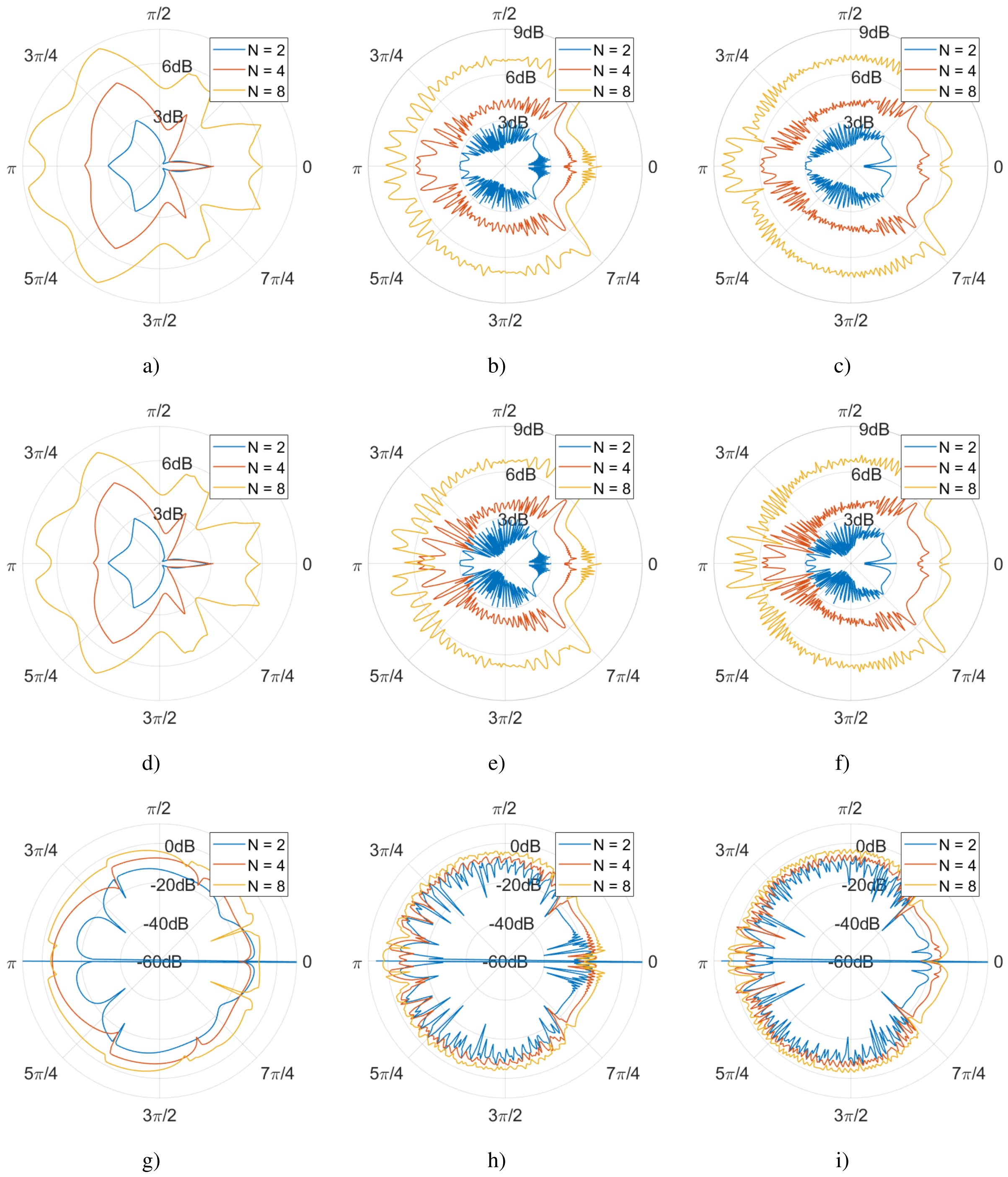

a) b) c)

d) e) f)

g) h) i)

Fig. 7: $G_{\text{mrc\_REAL}}$ as a function of the angle for an antenna located 10 cm away from the user model. The simulations for a plane wave of various frequencies impinging on a dielectric cylinder of 13.3 cm radius are shown. The leftmost column represents the simulations obtained for an incident wave of 1GHz. The centre column does so for a 30GHz wave while the right one depicts the 60GHz wave. The first row uses the dielectric model of the human cylinder while the second row uses a PEC one. The third row is the difference between the dielectric and PEC cylinders calculated using equation 26. Each tile depicts the gain of the antenna for 2, 4 and 8 elements.

to 5mm. In contrast, when going to 60GHz, d_{el} is further reduced to 2.5mm. This means that in the first gap, the antenna size is reduced by $\frac{1}{30}$ while in the second it is only reduced by $\frac{1}{2}$.

As opposed to the case of the 1GHz incident wave, the gain simulations for the 30GHz wave (Fig. 6 b) for dielectric and Fig. 6 e) for PEC) and for the 60GHz wave (Fig. 6 c) for dielectric and Fig. 6 f) for PEC) show big spikes in the gain around the cylinder. The reason for this can be explained again by the way in which the gain is defined. Since the reference point is always taken to be the center of the antenna, as the antena circles around the cylinder, the reference point will move between zones of maximum intensity, where constructive interference occurs, and minimum intensity, where destructive interference occurs. When the reference is at a minimum value, the perceived gain will be much higher than when the reference point is at a maximum, even though the total received power is more or less the same.

Moreover, it can be seen that the peaks present in the dielectric and PEC gains are located at the same angle for both the 30 GHz and 60GHz cases, however, the peaks seen in the PEC case are bigger than in the dielectric, especially in the case of the 4 and 8 element antennas. This is confirmed when looking at the ΔG plots, where the peaks again are located at the seme angles as their corresponding dielectric and PEC cases. This means that the interference pattern between the incident and scattered waves, i.e. the total field as seen in Fig. 5, is the same in the dielectric and PEC cases. However, the difference in the peaks suggests that the total field intensity is higher in the case of the PEC cylinder, especially in front of the cylinder, where the difference between peaks is maximum.

This can be explained by the fact that the PEC reflects all the power incident upon its surface in the form of scattered field. In contrast, in the case of the dilectric cylinder, part of th energy impinging on its surface is transmitted and disipated inside the dielectric material, meaning the scattered field has slightly less energy than in the PEC case. The result is that both cylinders create the same interference pattern but in the case of the PEC the intensity will be higher at the points where constructive interference happens, resulting in higher gains.

Note that, in the part in front of the cylinder, at angles roughly between 160 and 200 degrees, the peaks disappear. This is explained by the fact that the antenna is more or less perpendicular to the direction of propagation of the incident wave and therefore all elements will receive roughly the same power.

Lastly, in the case of the 30 GHz wave (Fig. 6 b) and e)), very big peaks can be observed in the close vecinity of the 0 degree angle. The explanation for this is similar to that of the high gains in the shaded region for the 1GHz case. Because the reference is taken at the center of the antenna, the reference point at this angle will be fully shaded by the cylinder resulting in a very low received power at this element. This means that as soon as the other elements receive some power, the gain can virtually become infinite, if no signal is received at the reference. In the case of the 60GHz simulation (Fig. 6 c) and f)), these peaks are not present anymore. The explanation for this is twofold. First, the blocking of the cylinder for this higher frequency is higher than in the previous case. Secondly, the antenna size is smaller meaning the antenna elements are more likely to receive a very similar close to zero value as the reference and thus result in a low gain.

Moving on to the plots seen in Fig. 7, the gains represented in this figure are those defined as $G_{\text{mrc\_REAL}}$, i.e. the reference is taken to be the element of the antenna receiving the maximum intensity. As in the case of Fig. 6, the plots in the first row (Fig. 7 a), b) and c)) are those obtained for the dielectric cylinder, the middle row (Fig. 7 d), e) and f)) is the PEC cylinder and the bottom row (Fig. 7 g), h) and i)) is the difference $\Delta G(\phi)$. Furthermore, the first column (Fig. 7 a), d) and g)) is for the simulations of 1GHz, the middle column (Fig. 7 b), e) and h)) is for 30Ghz and the third (Fig. 7 c), f) and i)) for 60GHz.

At first sight, big differences can be seen between the plots in Fig. 6 and Fig. 7. First of all, the big spikes previously present have almost disapeared. The reason for this is that the new definition of gain uses a dynamic selection of the reference power. This ensures that the reference power used is in the order of the total power received. In other words, if a lot of the elements of the antenna receive high signal intensites, they will all contribute to the gain. If, on the contrary, some elements are at points where destructive interference happens, these elements will contribute little to the gain, resulting in lower output values. This also ensures that no division by zero (or close to zero) can happen resulting in huge gains.

By using this new definition, in theory, the total power received by an antenna of N_{el} elements should be N_{el} times the power received by a single element. The gain depending on the number of antenna elements should scale accordingly. In other words, the gain of a 2-element antenna should be double that of a single element antenna, hence 3dB. The gain of a 4-element one should be double the gain of the previous example, 6dB and the 8 element antenna should result in a gain of 9dB. Of course, this assumes that all elements in the antenna are receiving the same power. Since the total field is not uniform in space, depending on the locations of the antenna elements and the definition of gain used, the values obtained can vary greately. By using the new gain definition $G_{\text{mrc\_REAL}}$, it is ensured that the gain is always below the maximum theoretical gain. This resuts in a more accurate representation of the received power depending on the angle and the number of antenna elements N_{el}

When looking at the plots for a 1GHz wave for dielectric (Fig. 7 a)) and PEC (Fig. 7 d)) cylinders it can be seen that the values obtained for angles between 90 an 270 degrees i.e. in front of the cylinder, are very similar to those in their counterpart of Fig. 6. In the region behind the cylinder, however, the gain has been greatly reduced. As was explained previously, at this frequency the antenna size is greater than the cylinder diameter. When using the previous definition of gain $G_{\text{mrc\_PERC.}}$, the reference was located behind the cylinder and hence receiving very low power values. With the new gain definition $G_{\text{mrc\_PERC.}}$ the reference is taken to be one of the elements that is not behind the cylinder and thus the gain is reduced.

The lowest gain values of Fig. 7 a) and Fig. 7 b) are located at angles of 45 and -45 degrees for the three cases of antenna elements plotted. The reason for this si that at this angle, a significant number of antenna elements are in the shaded region behind the cylinder and do not contribute much to the gain.

Next the 30GHz plots for dielectric (Fig. 7 b) and c)) and PEC (Fig. 7 e) and f)) cylinders will be looked at.

First of all, it can be seen that there are still relatively big spikes present in the plot of the 2-element antenna. The reason for this is that the reference power will always be one of the two elements. Depending on the power received by the other element, the gain can jump from 1dB to 3dB within a very small angle variation.

In the case of the four and eight element antennas, it can be seen that the gain obtained between the angles of 45 and 315 angles is more or less constant with small variations around the mean value. The plot looks very similar to its Fig. 6 counterpart if the big peaks were removed or reduced. The maximum gain values are obtained directly in front of the cylinder, at an approximate angle of 180 degrees. At this angle, the antenna is approximately perpendicular to the direction of propagation of the incident wave and all elements receive approximately the same power. This being the case, the gain at this angle gets close to its maximum theoretical value, especially in the 4 element antenna case.

The minimum gain is at an angle of approximately 40 and -40 degrees. At this angle, as in the case of Fig. 7 a) and d), part of the antenna is shielded by the cylinder and part of it is receiving the unimpeded signal from the source. Hence, the gain is lower than at other angles. In the angles around 0 degrees, the gain, although smaller than in other directoins, is still quite big. The reason for this is that all elements are fully shielded behind the cylinder but receiving approximately the same intensity, and hence, resulting in a relatively high gain.

Lastly, when looking at the plots of the difference beteen dielectric and PEC (Fig. 7 g), h) and i)) it can be seen that the difference stays below the the 0dB level at all angles except for 180 degrees in the case of the 30GHz and 60GHz plots in Fig. 7 h) and Fig. 7 i) respectively. Even at the angle of 180 degrees, the different is very low. As was stated earlier, these small differences are caused by the small dissipation of energy produced inside the dilectric cylinder. This proves that the PEC is a good approximation of the dielectric model.

So far, the main effects behind the antenna gain patterns have been explained. Many more plots for the diferent parameter combinations listed in Table VI can be seen in Apendix II. The same holds for the difference between dielectric and PEC cylinders ΔG as defined in equation (26) which can be found in Appendix III. These plots look very similar to the ones shown in Fig. 6 and Fig. 7. Therefore, the same explanations behind the patterns in these two figures apply to those plots. However, from the plots seen so far, not all the parameters involved in the simulations can be thoroughly analyzed. Only the influence of the frequency, the angle and the number of elements has been analyzed in depth.

In order to make a better analysis of the influence of each one of the remaining parameters as well as the performance of each one of the antenna figures of merit, the mean gain for each of the simulation cases is calculated using equation (27).

$$mean(G_{\text{mrc}}) = \frac{1}{360}\sum_{i=1}^{360} G_{mrc}(\phi_i) \tag{27}$$

The values of mean gain obtained as a function of the number of antenna elements are plotted in Fig. 8 for the case of $G_{\text{mrc\_PERC.}}$ and Fig. 9 for that of $G_{\text{mrc\_REAL}}$. Each one of the plots, shows the mean gain for both the dielectric and PEC cylinders for each of the three radii. In the first column (Fig. 8 a) and d) and Fig. 9 a) and d)) the mean values for a 1GHz wave are shown. The second column (Fig. 8 b) and e) and Fig. 9 b) and e)) shows the values obtained for 30GHz and the third column (Fig. 8 a) and d) and Fig. 9 a) and d)) shows those obtained for 60GHz. In the first row (Fig. 8 a), b) and c) and Fig. 9 a), b) and c)), the results of the simulation with $d_0 = 10$cm are shown wile the second row (Fig. 8 d), e) and f) and Fig. 9 d), e) and f)) shows those obtained for $d_0 = 20$cm. The maximum theoretical gain as described above is shown in all graphs with a black line to take as a reference.

To make a better analysis of the mean values represented in Fig. 8, a representative selection of the plotted values are listed in tables. The selected values from Fig. 8 a), b) and c), i.e. the $mean(G_{\text{mrc\_PERC.}})$ values for $d_0 = 10$cm are listed in Table VII. The selected values from Fig. 8 d), e) and f), i.e. the $mean(G_{\text{mrc\_PERC.}})$ values for $d_0 = 20$cm can be found in Table VIII. The selected values from Fig. 9a), b) and c) and Fig. 9 d), e) and f), i.e. the $mean(G_{\text{mrc\_PERC.}})$ values for $d_0 = 10$cm and $d_0 = 20$cm can be found in Table IX and Table X respectively.

When looking at the plots of $mean(G_{\text{mrc\_PERC.}})$ in Fig. 8 it can be seen that the average gain increases linearly with the number of antenna elements N_{el}, resulting in this logarithmic-like plot.

As the frequency increases, the gain is reduced. The mean gain drops by a bery big value between the 1GHz case Fig. 8 a) and d) and the 30GHz Fig. 8 b) and e) case.The perceived gain reaches its maximum values for a frequency of 1GHz Fig. 8 a) and d) as was expected after looking at the plots in Fig. 6 a) and d) where very high gains were reached in the region behind the cylinder. These high gains dominate over the gains at other angles resulting in much higher average gains.

A big gap can be seen between the case of the 1GHz simulation and that of 30GHz and 60GHz ones. For the case of the 60GHz wave Fig. 8 a) and d) , the average gain is further reduced but by a much lower margin than in the previous drop. For example, the average gain for an 8 element antenna in the case of a dielectric cylinder of radius 13.3cm and a $d_0 = 10$cm is 18.13dB for 1GHz, 10.82dB for 30GHz and 9.88dB for the 60GHz case. Similarly, the

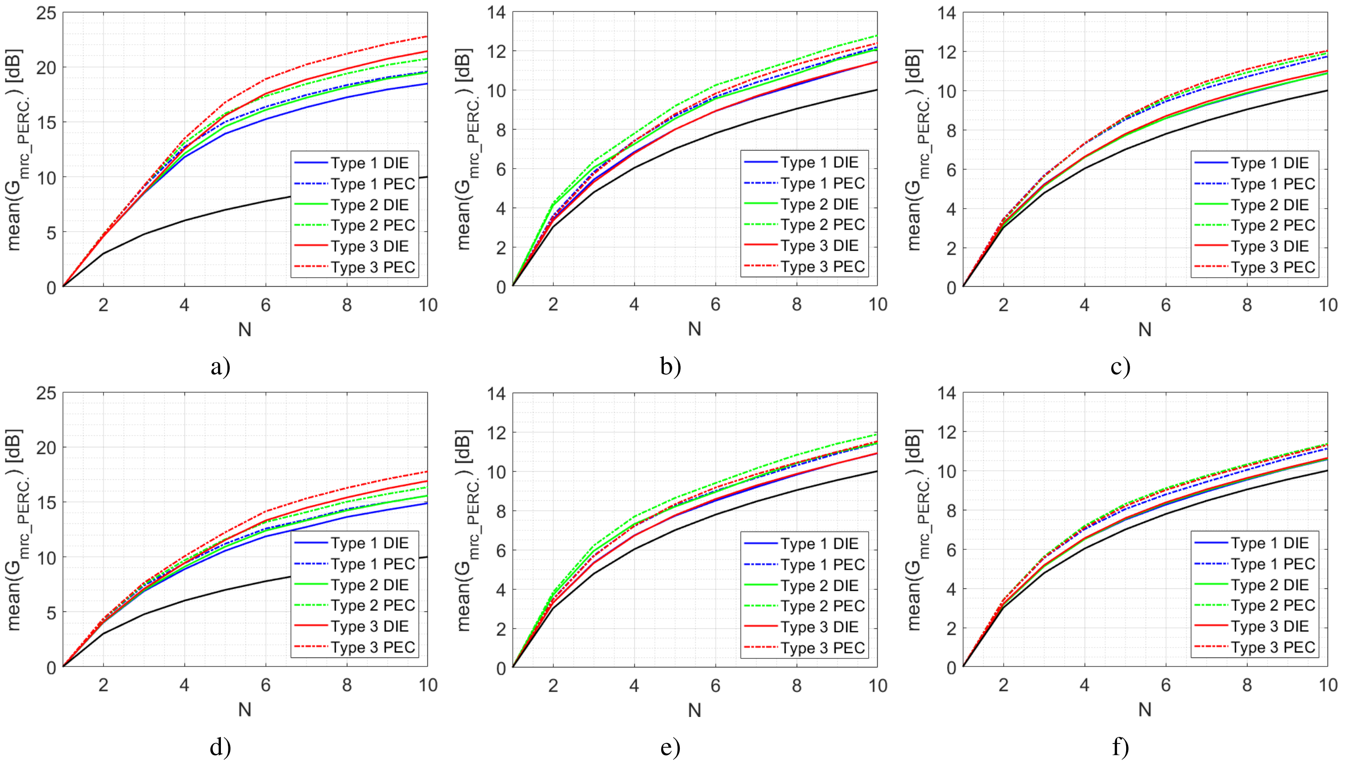

a) b) c)

d) e) f)

Fig. 8: Average value of the perceived gain of the MRC ($G_{mrc\_PERC.}$) around the cylinder. Each tile shows the three radii used for both dielectric and PEC cylinders. The first column is for 1GHz, the second for 30 GHz and the third for 60GHz. The top row simulates a distance between cylinder and antenna of 10 cm while the second one does so for 20cm.

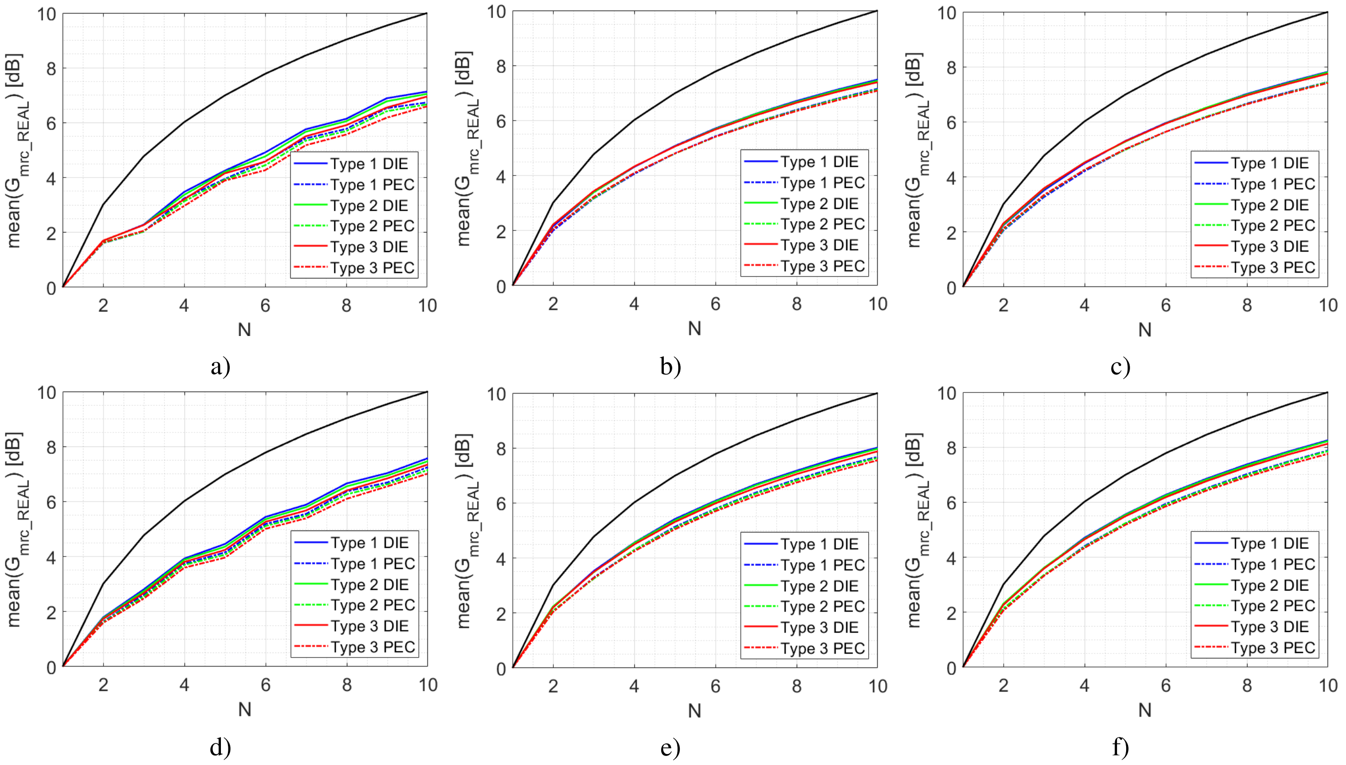

a) b) c)

d) e) f)

Fig. 9: Average value of the real gain of the MRC (G_{mrc_REAL}) around the cylinder. Each tile shows the three radii used for both dielectric and PEC cylinders. The first column is for 1GHz, the second for 30 GHz and the third for 60GHz. The top row simulates a distance between cylinder and antenna of 10 cm while the second one does so for 20cm.

TABLE VII: Selection of mean values of $G_{mrc\_PERC.}$ for $d_0 = 10$ cm

Radius	**Frequency**	**Cylinder**	N_{el}		
			2	**4**	**8**
Type 1	**1 GHz**	DIE	4.58	11.78	17.23
		PEC	4.76	12.70	18.34
	30 GHz	DIE	3.40	6.83	10.24
		PEC	3.59	7.40	10.98
	60 GHz	DIE	3.24	6.61	9.84
		PEC	3.46	7.28	10.70
Type 2	**1 GHz**	DIE	4.56	12.10	18.13
		PEC	4.76	13.08	19.39
	30 GHz	DIE	4.11	7.23	10.82
		PEC	4.23	7.77	11.54
	60 GHz	DIE	3.14	6.59	9.88
		PEC	3.37	7.30	10.91
Type 3	**1 GHz**	DIE	4.56	12.53	19.83
		PEC	4.73	13.48	21.19
	30 GHz	DIE	3.33	6.76	10.33
		PEC	3.51	7.38	11.29
	60 GHz	DIE	3.24	6.62	10.03
		PEC	3.43	7.31	11.08

TABLE VIII: Selection of mean values of $G_{mrc\_PERC.}$ for $d_0 = 20$ cm

Radius	**Frequency**	**Cylinder**	N_{el}		
			2	**4**	**8**
Type 1	**1 GHz**	DIE	4.02	8.87	13.63
		PEC	4.30	9.41	14.34
	30 GHz	DIE	3.30	6.73	9.82
		PEC	3.49	7.20	10.29
	60 GHz	DIE	3.20	6.50	9.53
		PEC	3.40	7.01	10.03
Type 2	**1 GHz**	DIE	4.04	9.09	14.22
		PEC	4.33	9.68	15.01
	30 GHz	DIE	3.69	7.30	10.40
		PEC	3.83	7.68	10.83
	60 GHz	DIE	3.17	6.50	9.56
		PEC	3.42	7.18	10.31
Type 3	**1 GHz**	DIE	4.08	9.43	15.39
		PEC	4.37	10.05	16.27
	30 GHz	DIE	3.29	6.71	9.86
		PEC	3.47	7.20	10.43
	60 GHz	DIE	3.21	6.55	9.61
		PEC	3.40	7.09	10.23

TABLE IX: Selection of mean values of G_{mrc_REAL} for $d_0 = 10$ cm

Radius	**Frequency**	**Cylinder**	N_{el}		
			2	**4**	**8**
Type 1	**1 GHz**	DIE	1.69	3.48	6.14
		PEC	1.61	3.24	5.78
	30 GHz	DIE	2.16	4.31	6.71
		PEC	2.00	4.06	6.39
	60 GHz	DIE	2.47	4.49	6.51
		PEC	2.05	4.21	6.67
Type 2	**1 GHz**	DIE	1.69	3.37	6.05
		PEC	1.62	3.13	5.69
	30 GHz	DIE	2.22	4.33	6.68
		PEC	2.07	4.09	6.36
	60 GHz	DIE	2.27	4.53	6.99
		PEC	2.09	4.26	6.65
Type 3	**1 GHz**	DIE	1.70	3.20	5.91
		PEC	1.64	2.96	5.57
	30 GHz	DIE	2.22	4.33	6.65
		PEC	2.05	4.10	6.35
	60 GHz	DIE	2.31	4.52	6.96
		PEC	2.12	4.26	6.64

TABLE X: Selection of mean values of G_{mrc_REAL} for $d_0 =$ 20 cm

Radius	**Frequency**	**Cylinder**	N_{el}		
			2	**4**	**8**
Type 1	**1 GHz**	DIE	1.79	3.93	6.66
		PEC	1.64	3.74	6.37
	30 GHz	DIE	2.21	4.56	7.17
		PEC	2.05	4.29	6.86
	60 GHz	DIE	2.27	4.71	7.38
		PEC	2.08	4.41	7.02
Type 2	**1 GHz**	DIE	1.77	3.89	6.55
		PEC	1.62	3.70	6.26
	30 GHz	DIE	2.24	4.55	7.13
		PEC	2.09	4.30	6.82
	60 GHz	DIE	2.31	4.68	7.34
		PEC	2.14	4.37	6.98
Type 3	**1 GHz**	DIE	1.74	3.81	6.40
		PEC	1.59	3.60	6.10
	30 GHz	DIE	2.20	4.49	7.05
		PEC	2.04	4.24	6.75
	60 GHz	DIE	2.27	4.65	7.27
		PEC	2.06	4.34	6.92

average gain of a 4 element antenna for a PEC cylinder of radius 16.6cm and $d_0 = 20$cm is 10.05dB at 1GHz, 7.20dB for 30GHz and 7.09 for 60GHz. This can be explained by looking at the plots in Fig. 6. In the case of the 30GHz, the gain is sligtly higer in fornt of the cylinder and much higher behind it than in the 60GHz case.

Moreover, as the frequency increases, the radius of the cylinder has less influence on the mean gain. In the case of an 8-element antenna at a distance $d_0 = 20$cm of a dielectirc cylinder with a carrier frequency of 1GHz has a mean gain of 13.63B if the radius is of Type 1, a gain of 14.22dB if the cylinder is of Type 2 and of 15.39dB if it is Type 3. For the same conditions but with an incident wave of frequency 60Ghz, the mean gains are 9.53dB, 9.56dB and 9.61dB for the cylinders of Type1, Type 2 and Type 3 respectively. Nevertheless, it is important to note that, as the radius of the cylinder increases, the mean gain increases as well.

Lastly, it can be seen that the gain for the $d_0 = 20$cm is slightly lower than that of the $d_0 = 10$cm. This effect is most clearly seen in the case of a 1GHz wave but is present at all three frequencies. As examples, in the case of a Type 2 PEC cylinder, an antenna with 8 elements and a carrier frequency of 30GHz, the gain is 11.54dB if $d_0 = 10$cm and 10.83dB in the case of $d_0 = 20$cm. In the case of a Type 3 DIE cylinder, an antenna with 2 elements and a carrier frequency of 1GHz, the gain is 4.56dB if $d_0 = 10$cm and 4.08dB in the case of $d_0 = 20$cm.

These same trends apply to all other combinations of values as can be seen in Table VII and Table VIII.

When looking at the plots of $mean(G_{\text{mrc\_REAL}})$ in Fig. 9 it can be seen that the average gain is now below the maximum theoretical value at all angles. Moreover, as in the case of Fig. 8, the mean gain increases linearly with the number of antenna elements N_{el}. The rest of the effects of the parameters mentioned above for $mean(G_{\text{mrc\_PERC.}})$ are mostly inverted for $mean(G_{\text{mrc\_REAL}})$.

Firstly, the average gain increases as the frequency increases. Taking the same examples as used for $mean(G_{\text{rms\_PERC.}})$, the average gain for an 8 element antenna in the case of a dielectric cylinder of radius 13.3cm and a $d_0 = 10$cm is 6.05dB for 1GHz, 6.68dB for 30GHz and 6.99dB for the 60GHz case. Similarly, the average gain of a 4 element antenna for a PEC cylinder of radius 16.6cm and $d_0 = 20$cm is 3.60dB at 1GHz, 4.24dB for 30GHz and 4.34 for 60GHz.

Secondly, although the influence of the cylinder radius still dicreases with increasing freqeuncy, the extent to which this is true is much less than in the previous case. Furthermore, as the radius of the cylinder increases, the mean gain decreases. Again, using the previous examples, an 8-element antenna at a distance $d_0 = 20$cm from a dielectirc cylinder with a frequency of 1GHz has a gain of 6.66dB for Type 1, of 6.55 for Type 2 and of 6.40 for Type 3. For the same conditions but with an incident wave of frequency 60Ghz, the mean gains are 7.38dB, 7.34dB and 7.27dB for the cylinders of Type1, Type 2 and Type 3 respectively.

Finally, the gain for the $d_0 = 20$cm is slightly higher than that of the $d_0 = 10$cm. The average gain of an 8-element antenna for a PEC cylinder of 13.3cm radius and an incident wave of 30GHz is 6.36dB for $d_0 = 10$cm and 6.83dB for $d_0 = 20$cm. In the case of a Type 3 DIE cylinder, an antenna with 2 elements and a carrier frequency of GHz, the gain is 1.70dB if $d_0 = 10$cm and 1.74dB in the case of $d_0 = 20$cm.

The last parameter altered in the simulations that needs to be analyzed is the difference between the equivalent dielectric model and the PEC cylinders. To better evaluate haw well the dielectric cylinder is approximated by the PEC cylinder, the root-mean-square value of the difference between them, called here RMSD, is calculated as seen in equation (28).

$$\text{RMSD} = \sqrt{\frac{1}{360}\sum_{i=1}^{360}(G_{\text{PEC}}(\phi_i) - G_{\text{DIE}}(\phi_i))^2} \qquad (28)$$

where the average is taken over 360 equally distributed angles at which the gains have been evaluated.

The values obtained for the RMSD of the perceived gain are shown in Fig. 10 while the ones obtained for real gain are shown in Fig. 11. These figures follow the same layout as the plots in Fig. 8 and Fig. 9. THe left column represents RMSD obtained for 1GHz, the center column represents those obtained for 30GHz and those in the right column represent the results of the simulation for 60GHz. The top row plots the values obtained for a $d_0 = 10$cm while the bottom row plots those obtained for $d_0 = 20$cm.

As in the case of Fig. 8 and Fig. 9, a representative selection of the values plotted in Fig. 10 and Fig. 11 is listed in Table , Table , Table and Table .

TABLE XI: Selection of RMSD values of $G_{mrc\_PERC.}$ for $d_0 = 10$ cm

Radius	**Frequency**	N_{el}		
		2	**4**	**8**
Type 1	**1 GHz**	-6.26	8.96	15.88
	30 GHz	-5.36	3.21	7.93
	60 GHz	-4.63	3.80	8.24
Type 2	**1 GHz**	-6.28	9.56	17.41
	30 GHz	-3.70	3.74	8.61
	60 GHz	-4.73	4.02	9.47
Type 3	**1 GHz**	-6.94	9.70	19.71
	30 GHz	-5.14	3.85	9.48
	60 GHz	-4.77	4.18	9.64

TABLE XII: Selection of RMSD values of $G_{mrc\_PERC.}$ for $d_0 = 20$ cm

Radius	**Frequency**	N_{el}		
		2	**4**	**8**
Type 1	**1 GHz**	-4.16	2.55	9.53
	30 GHz	-5.45	2.00	4.99
	60 GHz	-5.00	2.35	5.06
Type 2	**1 GHz**	-4.02	3.14	10.82
	30 GHz	-5.20	2.14	5.67
	60 GHz	-4.47	3.30	6.90
Type 3	**1 GHz**	-3.78	3.68	12.81
	30 GHz	-5.79	2.18	6.36
	60 GHz	-5.40	2.51	6.47

When looking at the plots in Fig. 10 not much new information can be gained than that already seen in previous figures. First, the RMSD value increases with frequency. This is particularly the case in the case of a 1GHz wave (Fig. 10 a) and b)). As was explained previously, this is caused by the big gains in the region shielded by the cylinder.

The error for the 30 GHz and 60GHz simulations at a given distance show very similar values. For example, a 4 element antenna, at a distance $d_0 = 10$cm from a Type 2 cylinder results in an RMSD of 3.74dB for 30GHz and of 4.02dB for 60GHz.

A big drop in the error can be seen when d_0 is increased to 20cm. For example, for a Type 3 cylinder, an 8 element

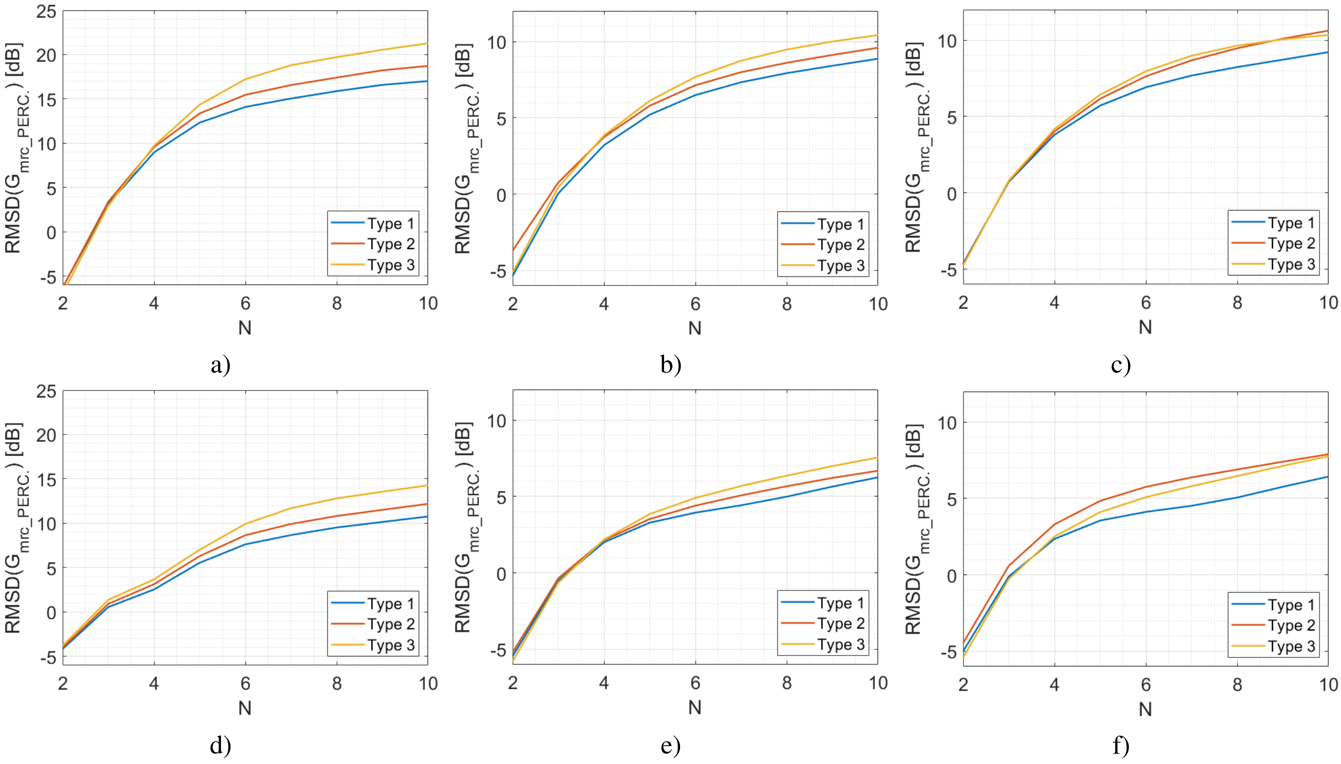

a) b) c)

d) e) f)

Fig. 10: Values of RMSD calculated for the perceived gain ($G_{mrc\_PERC.}$). Each tile shows the three radii. The first column is for 1GHz, the second for 30 GHz and the third for 60GHz. The top row simulates a distance between cylinder and antenna of 10 cm while the second one does so for 20cm.

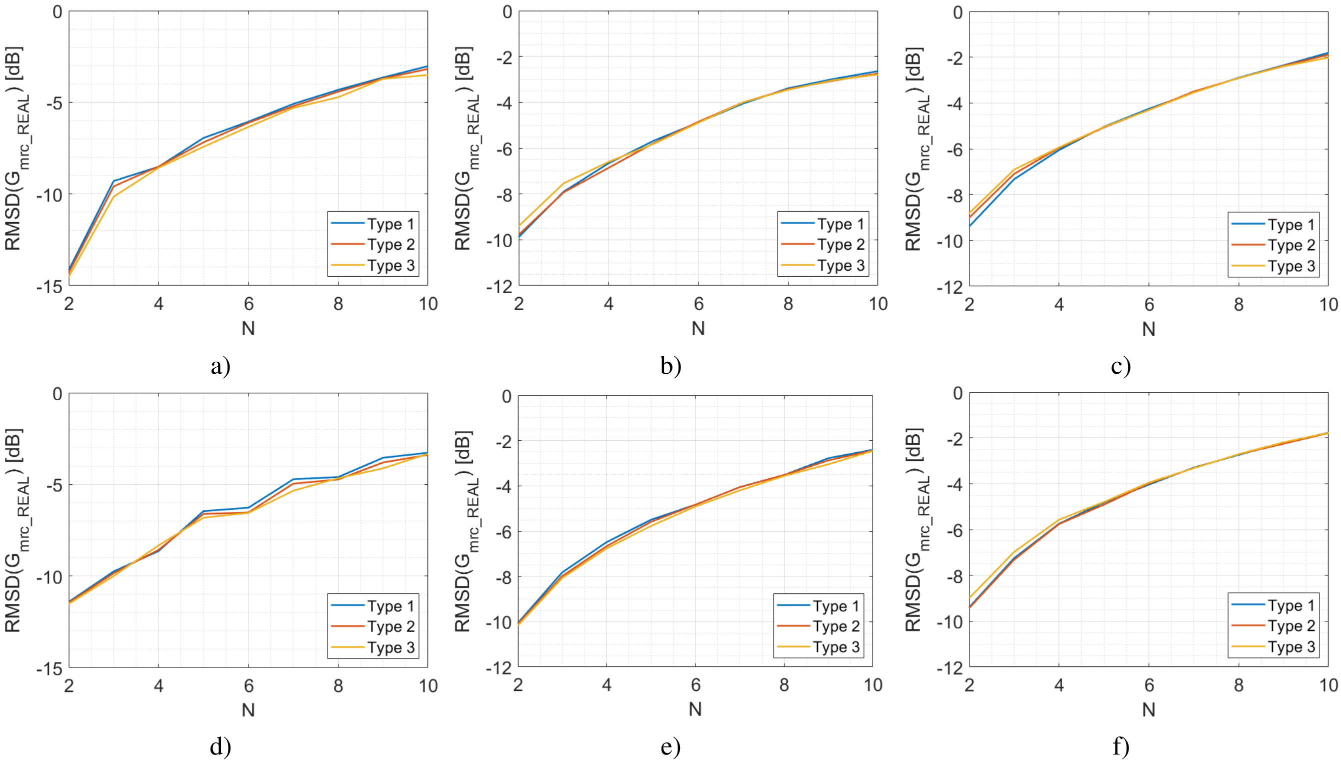

a) b) c)

d) e) f)

Fig. 11: Values of RMSD calculated for the real gain (G_{mrc_REAL}). Each tile shows the three radii. The first column is for 1GHz, the second for 30 GHz and the third for 60GHz. The top row simulates a distance between cylinder and antenna of 10 cm while the second one does so for 20cm.

TABLE XIII: Selection of RMSD values of G_{mrc_REAL} for $d_0 = 10$ cm

Radius	**Frequency**	N_{el}		
		2	**4**	**8**
Type 1	**1 GHz**	-14.16	-8.52	-4.32
	30 GHz	-9.88	-6.66	-3.39
	60 GHz	-9.39	-6.05	-2.90
Type 2	**1 GHz**	-14.30	-8.50	-4.42
	30 GHz	-9.78	-6.86	-3.43
	60 GHz	-9.01	-5.96	-2.92
Type 3	**1 GHz**	-14.52	-8.57	-4.72
	30 GHz	-9.40	-6.60	-3.45
	60 GHz	-8.81	-5.94	-2.91

TABLE XIV: Selection of RMSD values of G_{mrc_REAL} for $d_0 = 20$ cm

Radius	**Frequency**	N_{el}		
		2	**4**	**8**
Type 1	**1 GHz**	-11.41	-8.63	-4.60
	30 GHz	-10.06	-6.49	-3.52
	60 GHz	-9.39	-5.75	-2.74
Type 2	**1 GHz**	-11.45	-8.57	-4.73
	30 GHz	-10.10	-6.66	-3.52
	60 GHz	-9.43	-5.76	-2.72
Type 3	**1 GHz**	-11.52	-8.33	-4.66
	30 GHz	-10.17	-6.76	-3.56
	60 GHz	-8.99	-5.57	-2.71

antenna and a carrier frequency of 60GHz, the error is 9.64dB for $d_0 = 10$cm and 6.47dB for $d_0 = 10$cm

In the case of the plots obtained for the RMSD of the $G_{\mathrm{mrc\_REAL}}$, seen in Fig. 10 not many observations can be made from the graphs. It can be seen that the RMSD for this gain definition stays below -2dB except for the case where a 10 element antenna is subgect to a 60GHz frequency.

Furthermore, the RMSD is seen to increase with the number of elements N_{el}. The reason for this, most likely, is that the total received power is greater for higher N_{el}, meaning that a small relative difference can result in higher RMSD values when using the dB scale.

Finally, it is important to know that the RMSD values for all three cylinder types is esentially the same.

VI. CONCLUSIONS

In this paper, the scattering problem by a cylinder of both PEC and dielectric material has been analyzed. The MRC output of a ULA antenna in the close vecinity of said cylinder has been studied.

The main theory behind the dielectric propeties of human tissues has been presented and an equivalent dielectric model has been created using two dielectric mixing methods based on a widely used model of thickness proportions. It has been shown that the two methods used produce rather similar equivalent dielectric properties for the frequency range being simulated.

The total field around the cylinder, result of the sum of the incident and scattered field, has been shown and the main differences between dielectric and PEC solutions have been analyzed. Of particular importance is the blocking effect appreciated at frequencies of 30GHz and beyond.

Two performance metrics have been used to study the output of the ULA, one using its center element as a reference and another using the element receiving maximum power. Depending on which of these gains is used, the output can vary grately.

Special care needs to be taken if the central element is taken as a reference as it can result in disproportionate gains unrelated to the total power received by the antenna. Therefore, taking the element with maximum received power as the reference seems to be a better metric.

The influence of frequency, radius of the cylinder, number of elements in the linear array and distance between cylinder and array have been studied and it has been shown that, although the effect of each one can be analyzed individually, the full picture can only be understood when all are taken into account.

Finally, it has been shown that a dielectric cylinder human model can be approximated by a PEC cylinder of equal dimensions.

VII. APPENDIX I

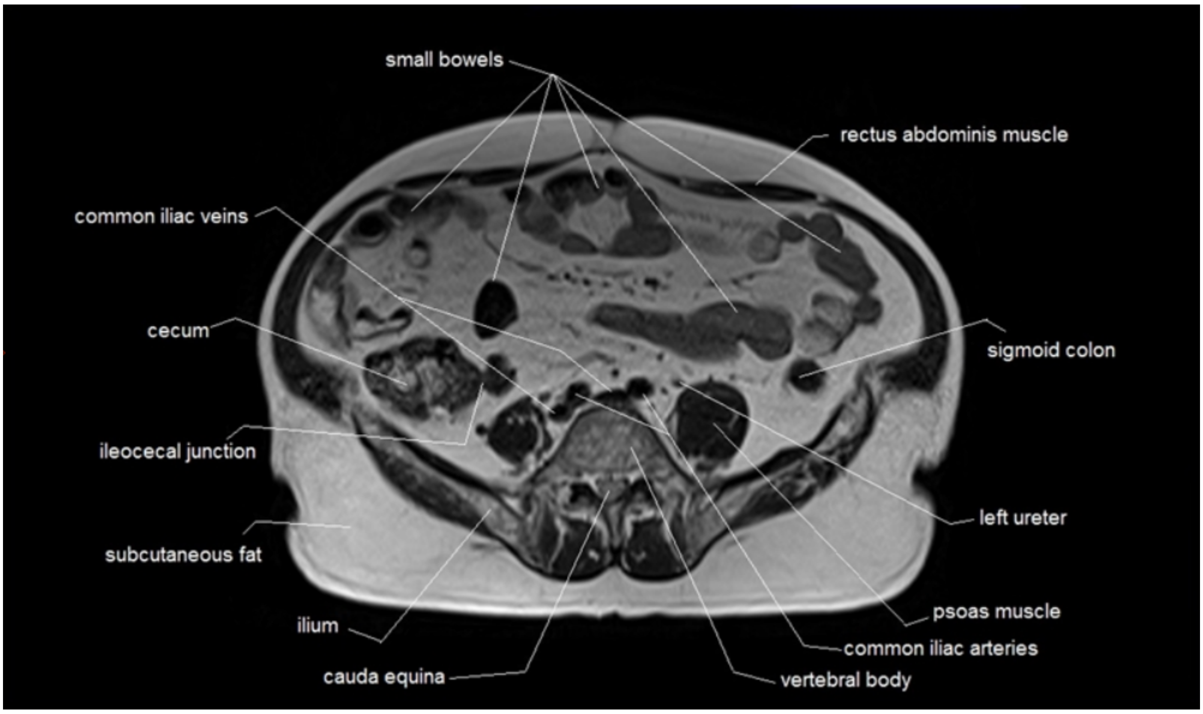

Fig. 12: MRI scanner image of the abdominal axial crossection of a human body [24]

VIII. Appendix II

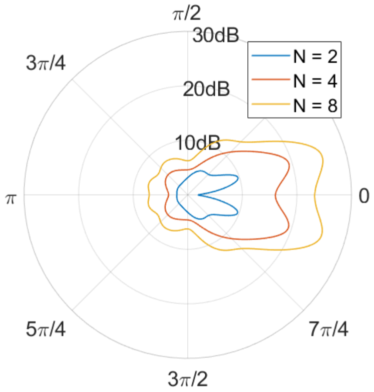

Fig. 13: a)

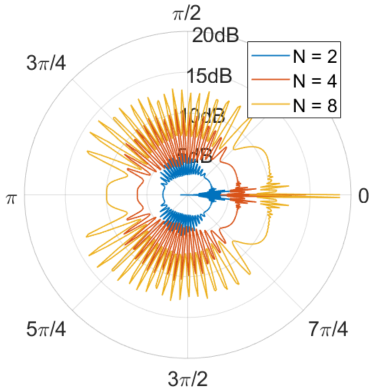

Fig. 14: b)

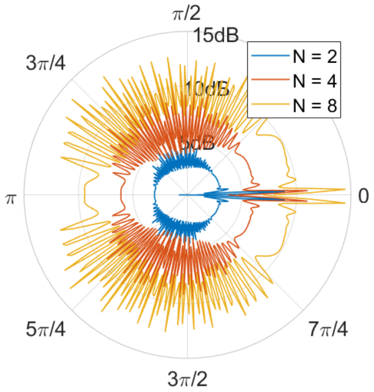

Fig. 15: c)

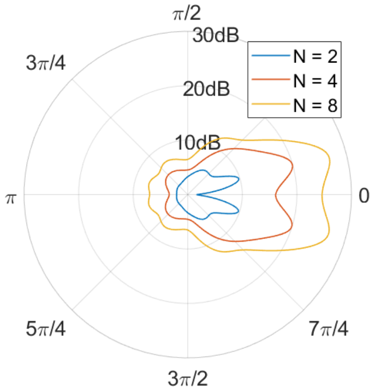

Fig. 16: d)

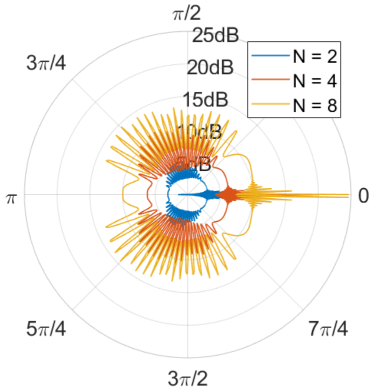

Fig. 17: e)

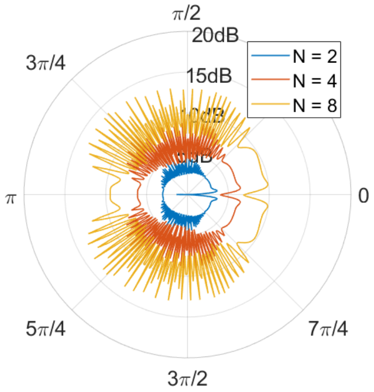

Fig. 18: f)

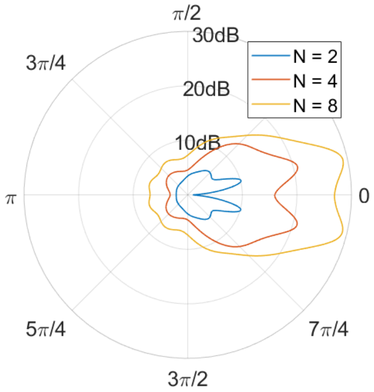

Fig. 19: g)

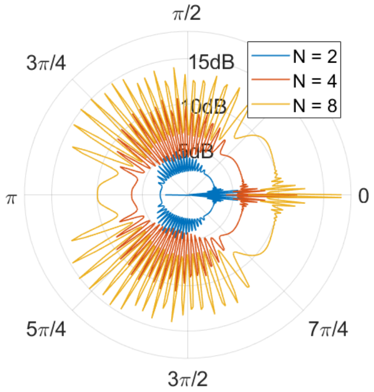

Fig. 20: h)

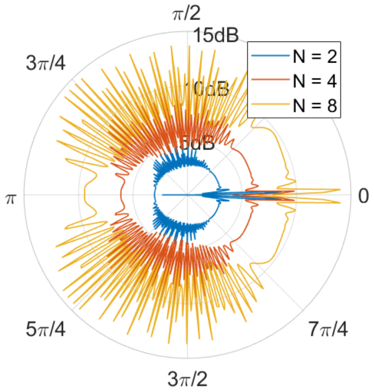

Fig. 21: i)

Fig. 22: $G_{\text{mrc\_PERC.}}$ as a function of the angle for $d_0 = 10\text{cm}$. The simulations for a plane wave of various frequencies impinging on a dielectric cylinder of various radii are shown. The leftmost column represents the simulations obtained for an incident wave of 1GHz. The centre column does so for a 30GHz wave while the right one depicts the 60GHz wave. The first row uses a Type 1 cylinder (11 cm), the second a Type 2 cylinder (13.3 cm) and the third row a Type 3 one (16 cm). Each tile depicts the gain of the antenna for 2, 4 and 8 elements.

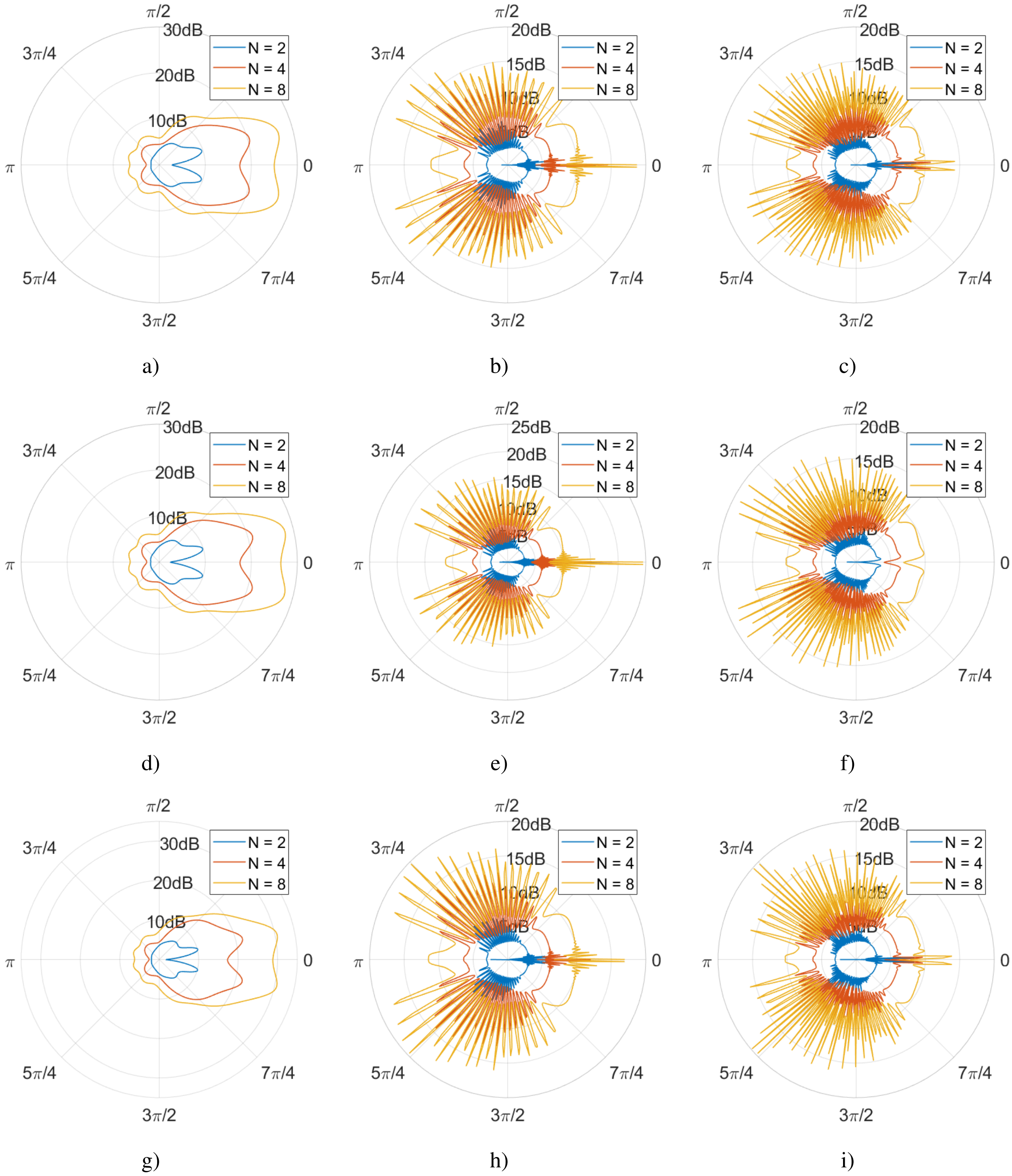

a) b) c)

d) e) f)

g) h) i)

Fig. 23: $G_{\mathrm{mrc\_PERC.}}$ as a function of the angle for $d_0 = 10$cm. The simulations for a plane wave of various frequencies impinging on a PEC cylinder of various radii are shown. The leftmost column represents the simulations obtained for an incident wave of 1GHz. The centre column does so for a 30GHz wave while the right one depicts the 60GHz wave. The first row uses a Type 1 cylinder (11 cm), the second a Type 2 cylinder (13.3 cm) and the third row a Type 3 one (16 cm). Each tile depicts the gain of the antenna for 2, 4 and 8 elements.

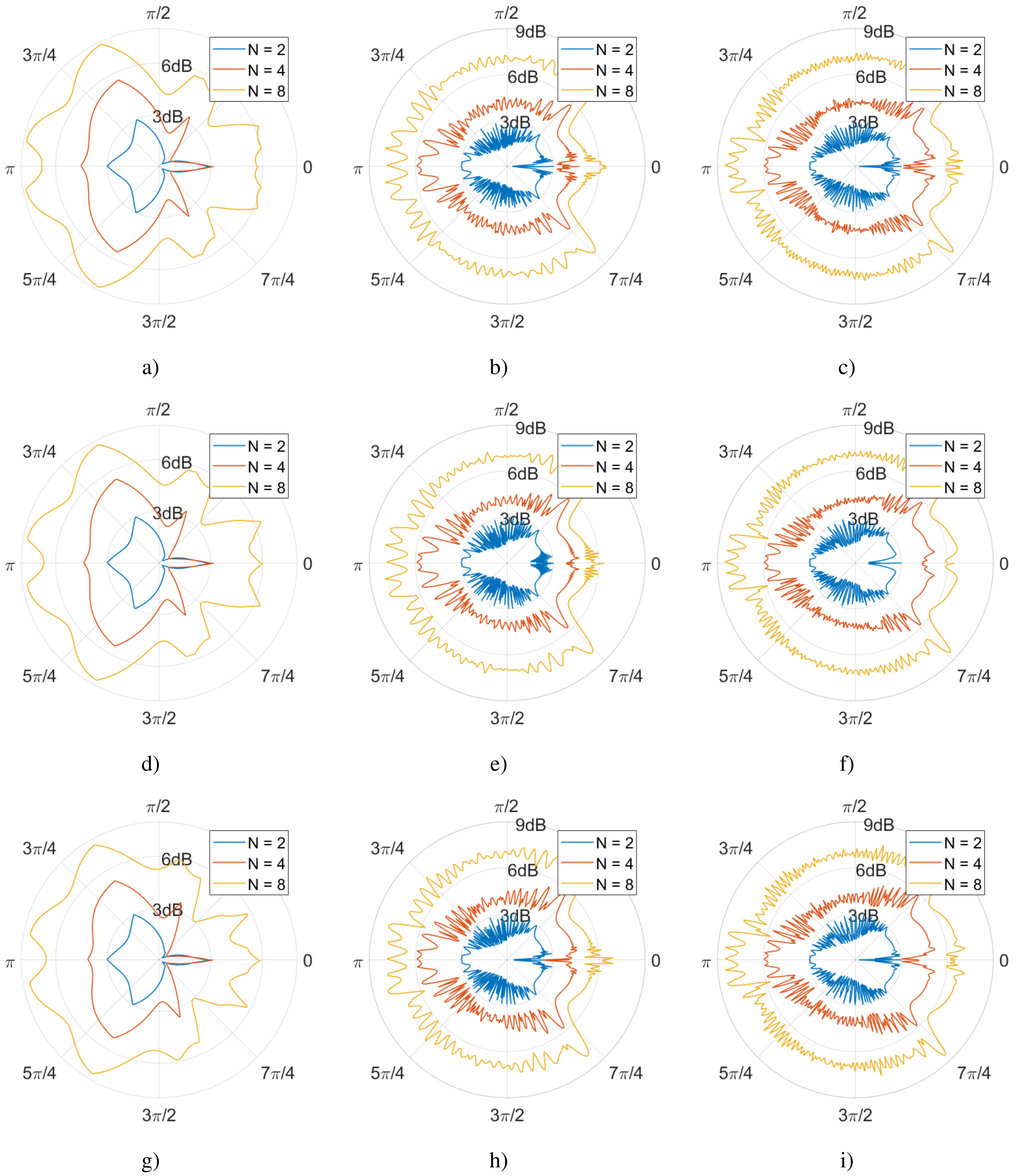

a) b) c)

d) e) f)

g) h) i)

Fig. 24: $G_{\mathrm{mrc\_REAL}}$ as a function of the angle for $d_0 = 10$cm. The simulations for a plane wave of various frequencies impinging on a dielectric cylinder of various radii are shown. The leftmost column represents the simulations obtained for an incident wave of 1GHz. The centre column does so for a 30GHz wave while the right one depicts the 60GHz wave. The first row uses a Type 1 cylinder (11 cm), the second a Type 2 cylinder (13.3 cm) and the third row a Type 3 one (16 cm). Each tile depicts the gain of the antenna for 2, 4 and 8 elements.

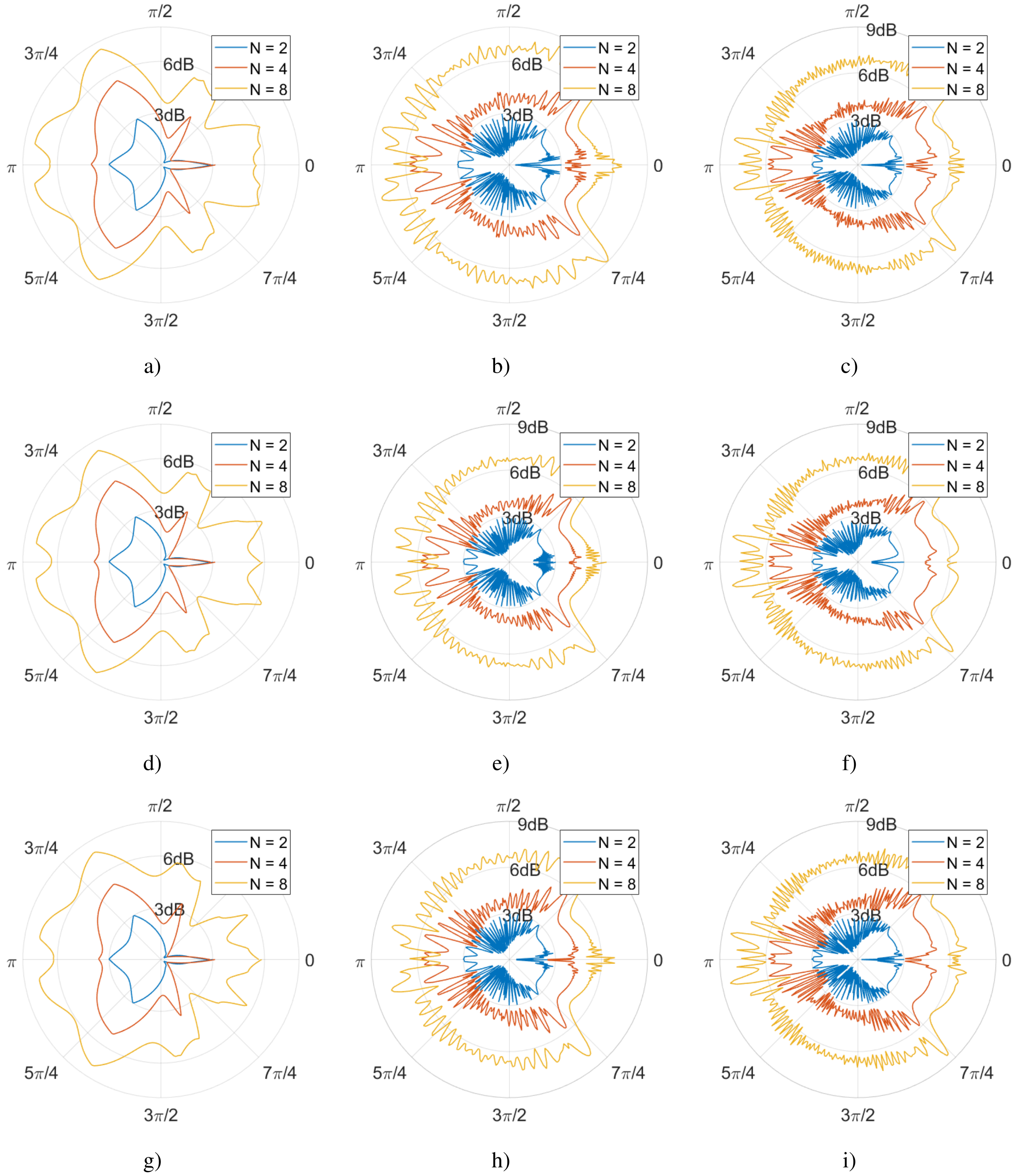

Fig. 25: $G_{\text{mrc\_REAL}}$ as a function of the angle for $d_0 = 10$cm. The simulations for a plane wave of various frequencies impinging on a PEC cylinder of various radii are shown. The leftmost column represents the simulations obtained for an incident wave of 1GHz. The centre column does so for a 30GHz wave while the right one depicts the 60GHz wave. The first row uses a Type 1 cylinder (11 cm), the second a Type 2 cylinder (13.3 cm) and the third row a Type 3 one (16 cm). Each tile depicts the gain of the antenna for 2, 4 and 8 elements.

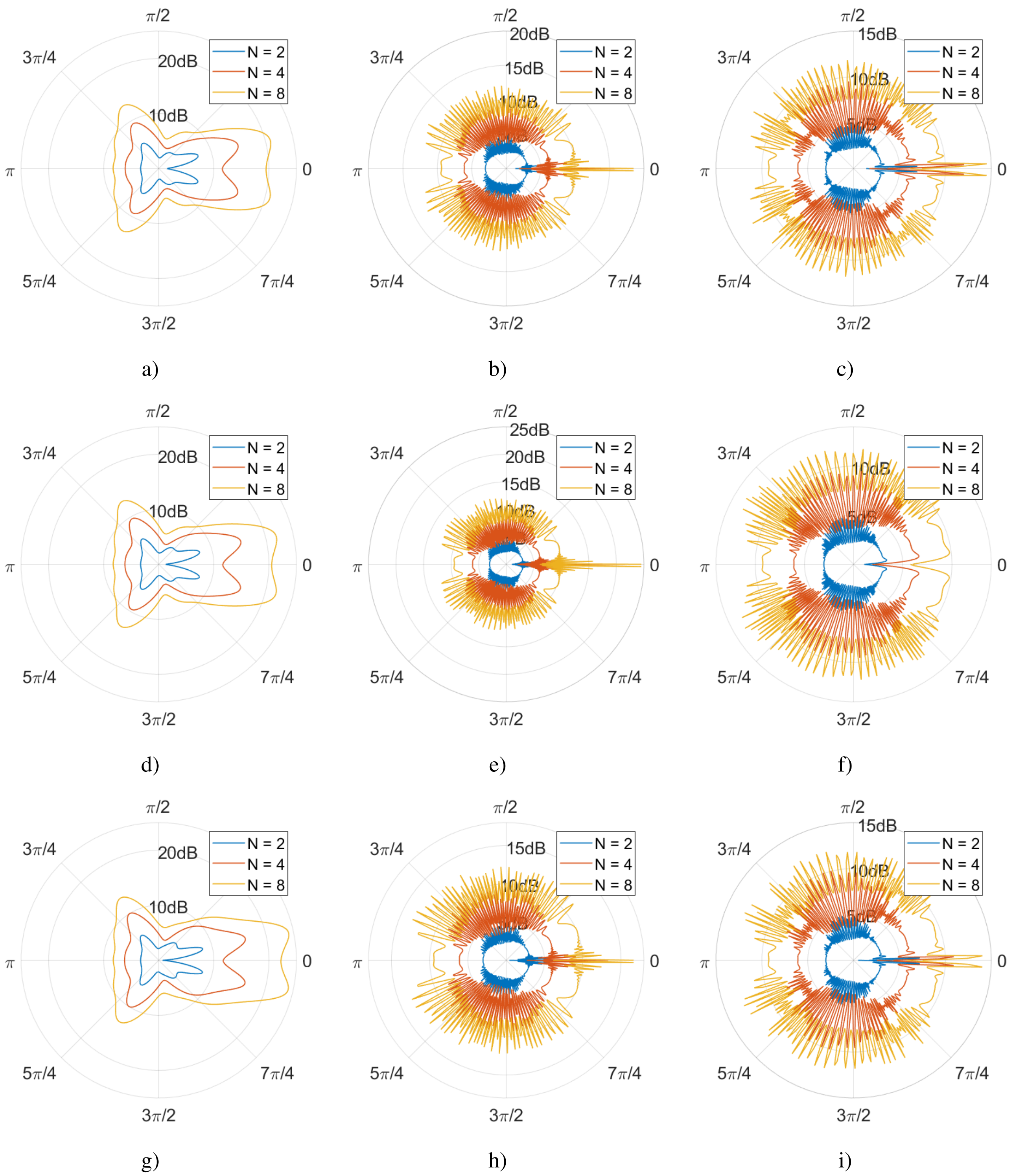

a) b) c)

d) e) f)

g) h) i)

Fig. 26: $G_{\mathrm{mrc\_PERC.}}$ as a function of the angle for $d_0 = 20$cm. The simulations for a plane wave of various frequencies impinging on a dielectric cylinder of various radii are shown. The leftmost column represents the simulations obtained for an incident wave of 1GHz. The centre column does so for a 30GHz wave while the right one depicts the 60GHz wave. The first row uses a Type 1 cylinder (11 cm), the second a Type 2 cylinder (13.3 cm) and the third row a Type 3 one (16 cm). Each tile depicts the gain of the antenna for 2, 4 and 8 elements.

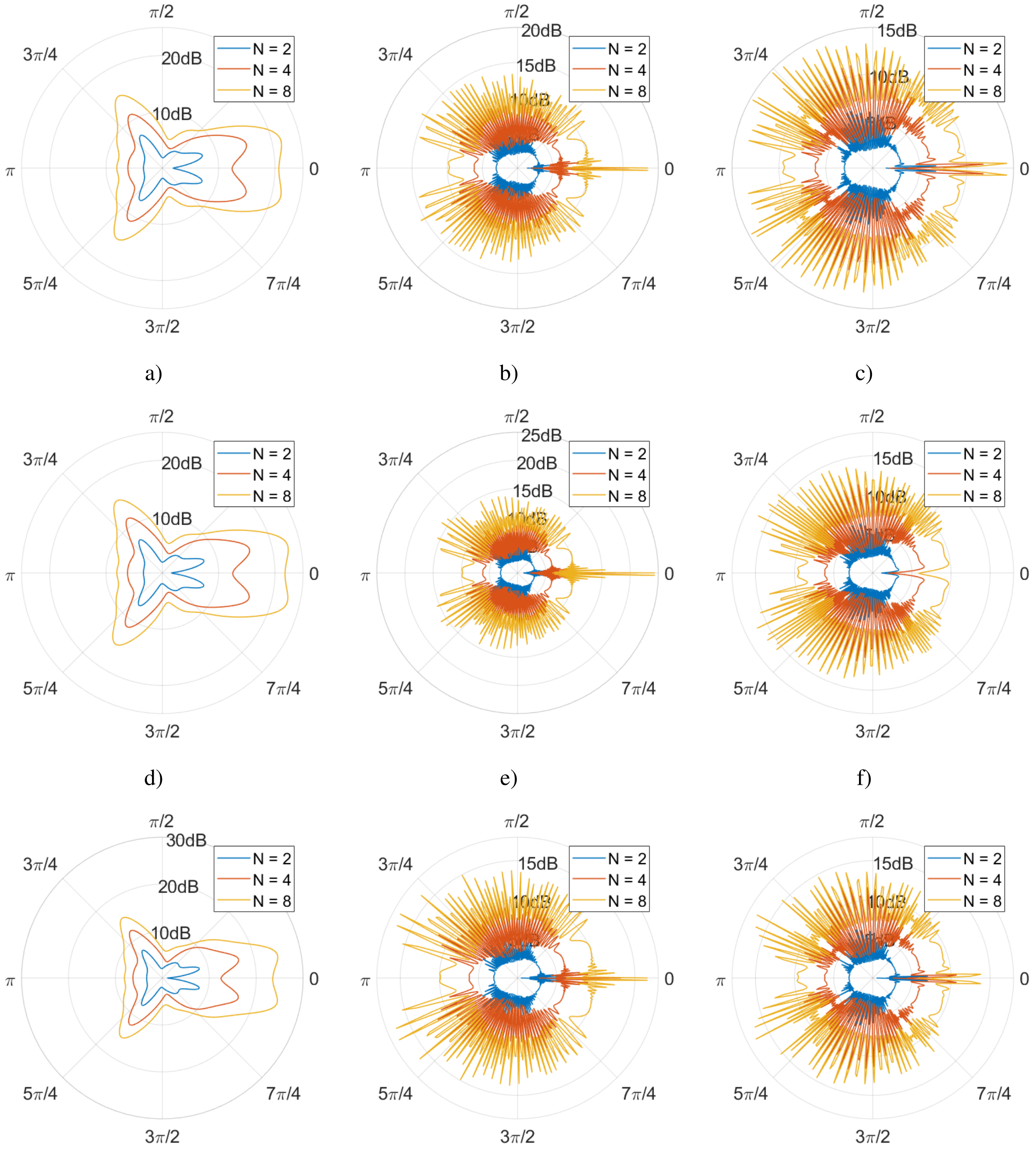

a) b) c)

d) e) f)

g) h) i)

Fig. 27: $G_{\text{mrc\_PERC.}}$ as a function of the angle for $d_0 = 20$cm. The simulations for a plane wave of various frequencies impinging on a PEC cylinder of various radii are shown. The leftmost column represents the simulations obtained for an incident wave of 1GHz. The centre column does so for a 30GHz wave while the right one depicts the 60GHz wave. The first row uses a Type 1 cylinder (11 cm), the second a Type 2 cylinder (13.3 cm) and the third row a Type 3 one (16 cm). Each tile depicts the gain of the antenna for 2, 4 and 8 elements.

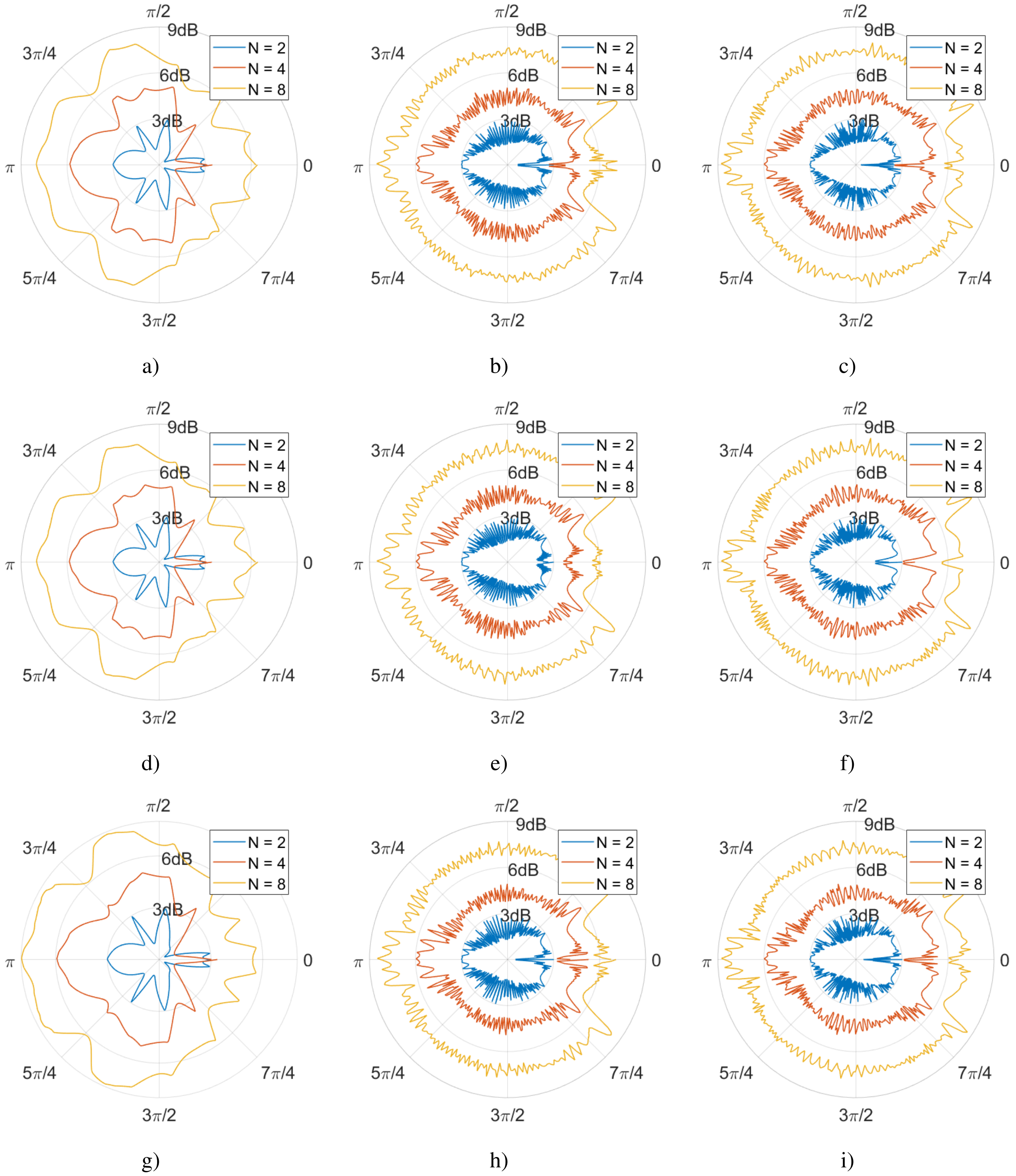

a) b) c)

d) e) f)

g) h) i)

Fig. 28: $G_{\text{mrc\_REAL}}$ as a function of the angle for $d_0 = 20$cm. The simulations for a plane wave of various frequencies impinging on a dielectric cylinder of various radii are shown. The leftmost column represents the simulations obtained for an incident wave of 1GHz. The centre column does so for a 30GHz wave while the right one depicts the 60GHz wave. The first row uses a Type 1 cylinder (11 cm), the second a Type 2 cylinder (13.3 cm) and the third row a Type 3 one (16 cm). Each tile depicts the gain of the antenna for 2, 4 and 8 elements.

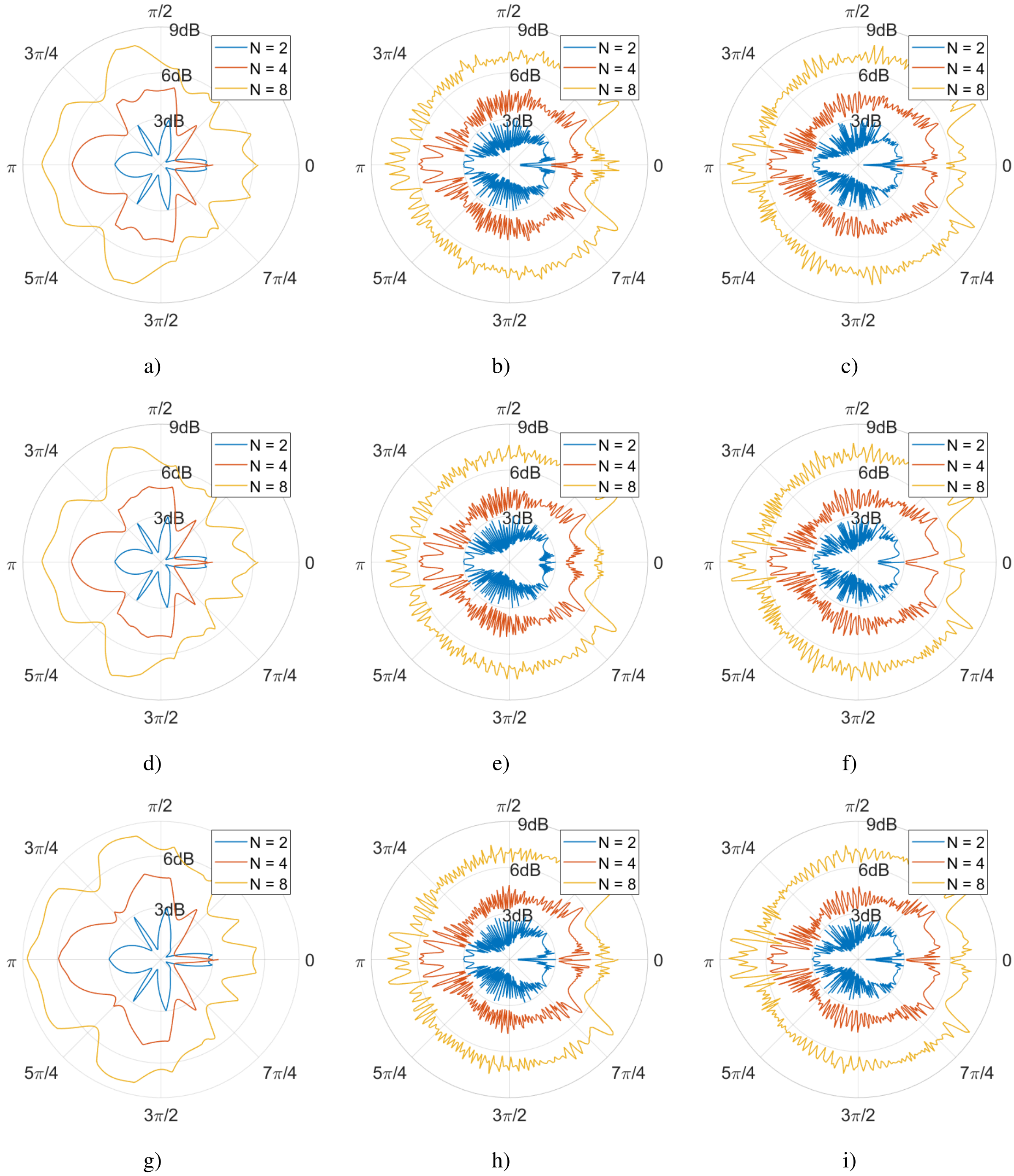

a) b) c)

d) e) f)

g) h) i)

Fig. 29: $G_{\mathrm{mrc\_REAL}}$ as a function of the angle for $d_0 = 20\text{cm}$. The simulations for a plane wave of various frequencies impinging on a PEC cylinder of various radii are shown. The leftmost column represents the simulations obtained for an incident wave of 1GHz. The centre column does so for a 30GHz wave while the right one depicts the 60GHz wave. The first row uses a Type 1 cylinder (11 cm), the second a Type 2 cylinder (13.3 cm) and the third row a Type 3 one (16 cm). Each tile depicts the gain of the antenna for 2, 4 and 8 elements.

IX. Appendix III

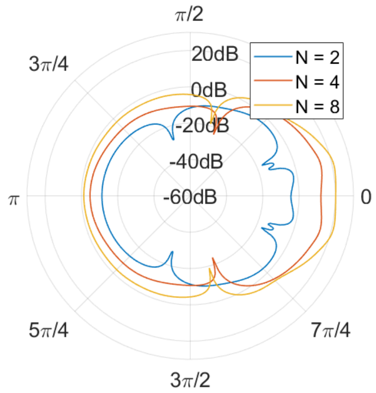

Fig. 30: a)

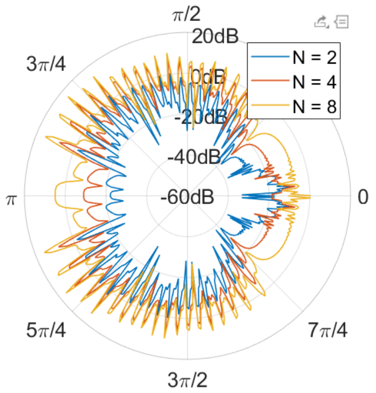

Fig. 31: b)

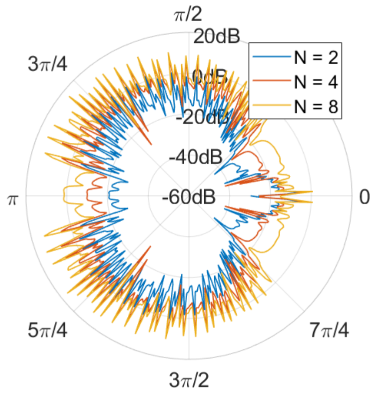

Fig. 32: c)

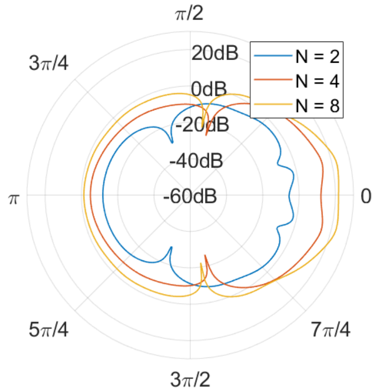

Fig. 33: a)

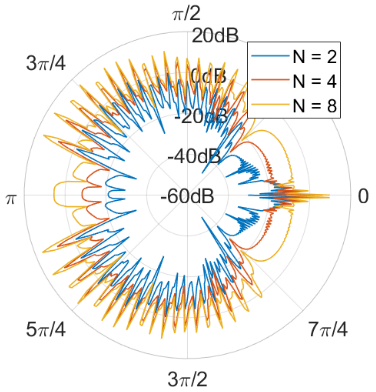

Fig. 34: b)

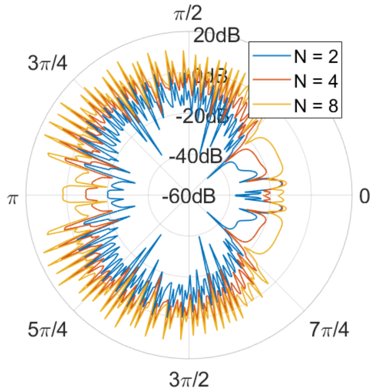

Fig. 35: c)

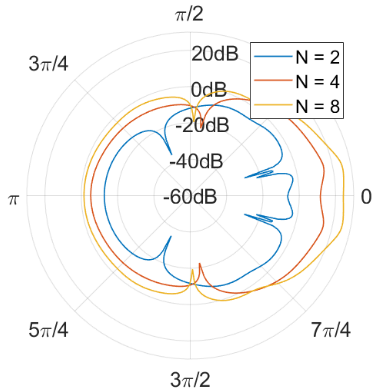

Fig. 36: a)

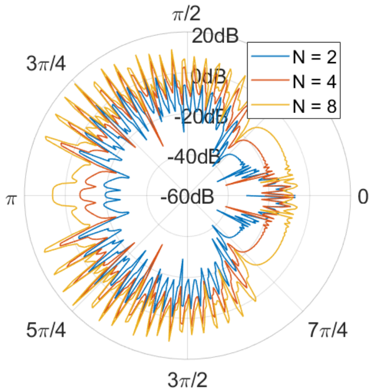

Fig. 37: b)

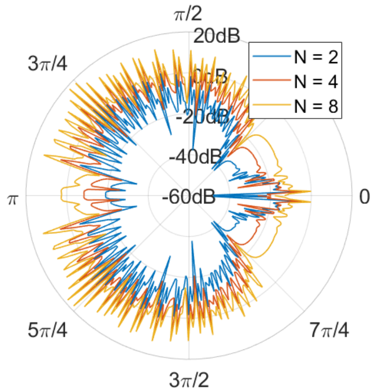

Fig. 38: c)

Fig. 39: ΔG of the perceived gain as a function of the angle for an antenna located 10 cm away from the user model. The simulations for a plane wave of various frequencies are shown. The leftmost column represents the simulations obtained for an incident wave of 1GHz. The centre column does so for a 30GHz wave while the right one depicts the 60GHz wave. The first row uses a Type 1 cylinder (11 cm), the second a Type 2 cylinder (13.3 cm) and the third row a Type 3 one (16 cm). Each tile depicts the gain of the antenna for 2, 4 and 8 elements.

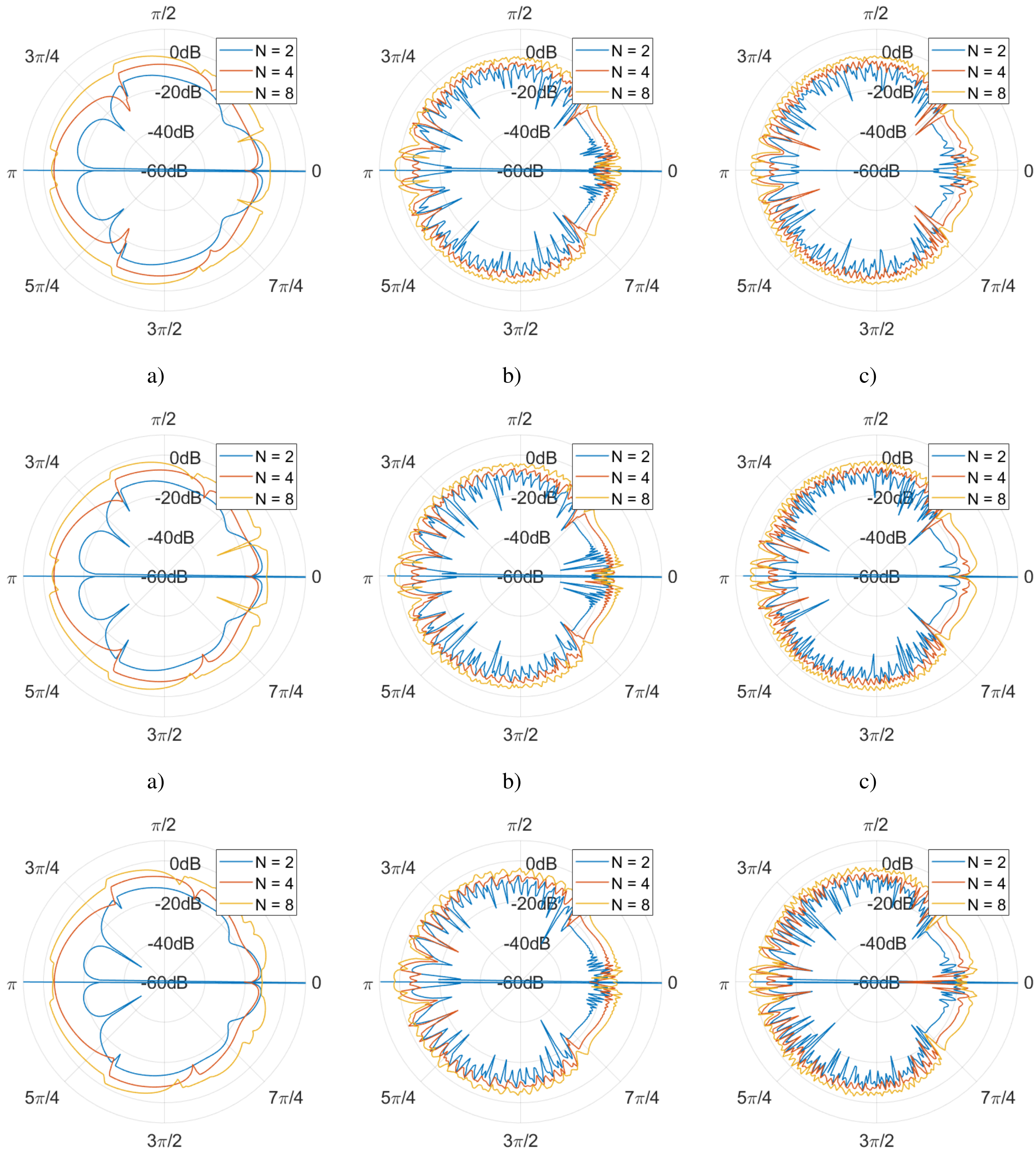

a) b) c)

a) b) c)

a) b) c)

Fig. 40: ΔG of the real gain as a function of the angle for an antenna located 10 cm away from the user model. The simulations for a plane wave of various frequencies are shown. The leftmost column represents the simulations obtained for an incident wave of 1GHz. The centre column does so for a 30GHz wave while the right one depicts the 60GHz wave. The first row uses a Type 1 cylinder (11 cm), the second a Type 2 cylinder (13.3 cm) and the third row a Type 3 one (16 cm). Each tile depicts the gain of the antenna for 2, 4 and 8 elements.

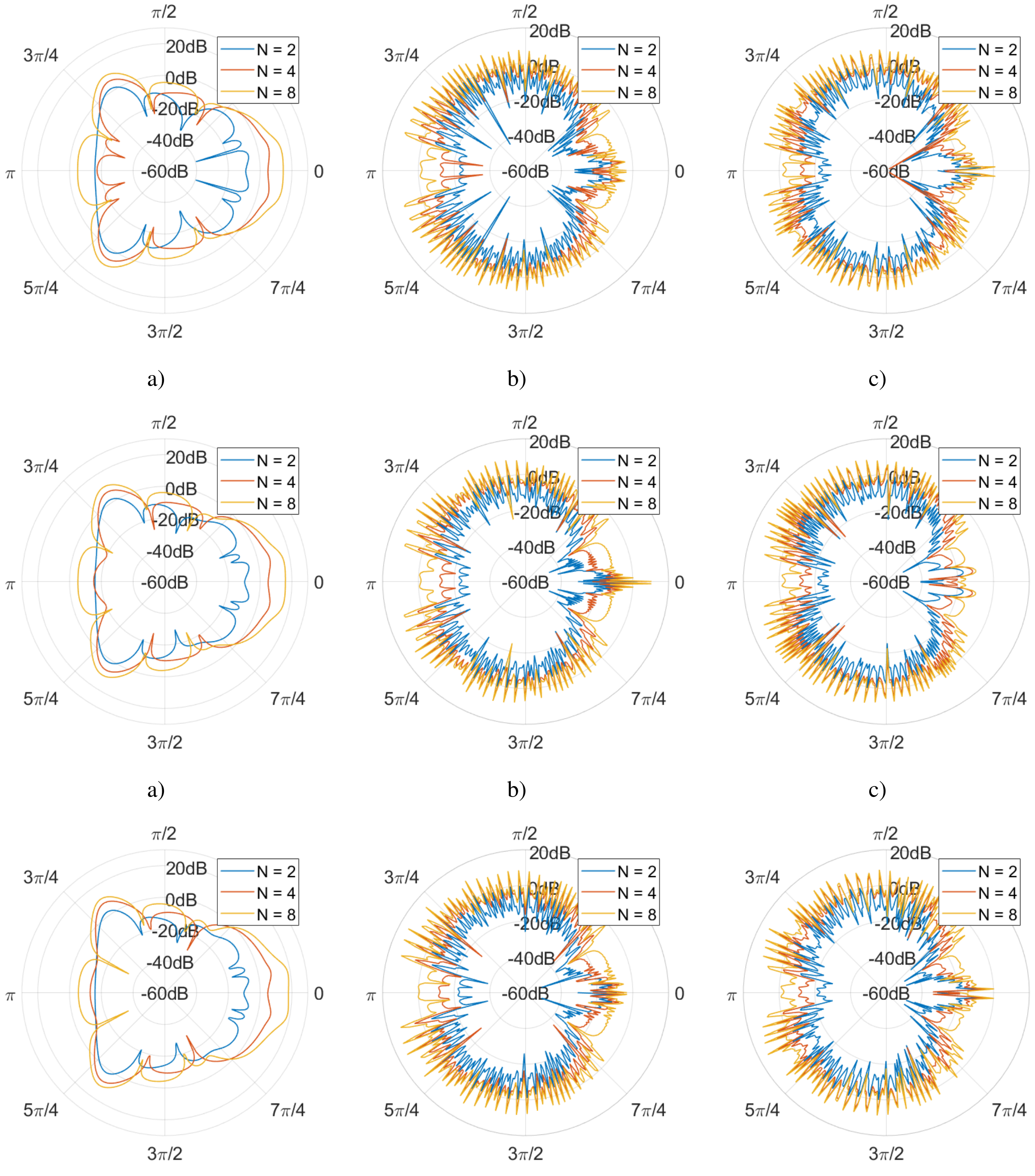

a) b) c)

a) b) c)

a) b) c)

Fig. 41: ΔG of the perceived gain as a function of the angle for an antenna located 20 cm away from the user model. The simulations for a plane wave of various frequencies are shown. The leftmost column represents the simulations obtained for an incident wave of 1GHz. The centre column does so for a 30GHz wave while the right one depicts the 60GHz wave. The first row uses a Type 1 cylinder (11 cm), the second a Type 2 cylinder (13.3 cm) and the third row a Type 3 one (16 cm). Each tile depicts the gain of the antenna for 2, 4 and 8 elements.

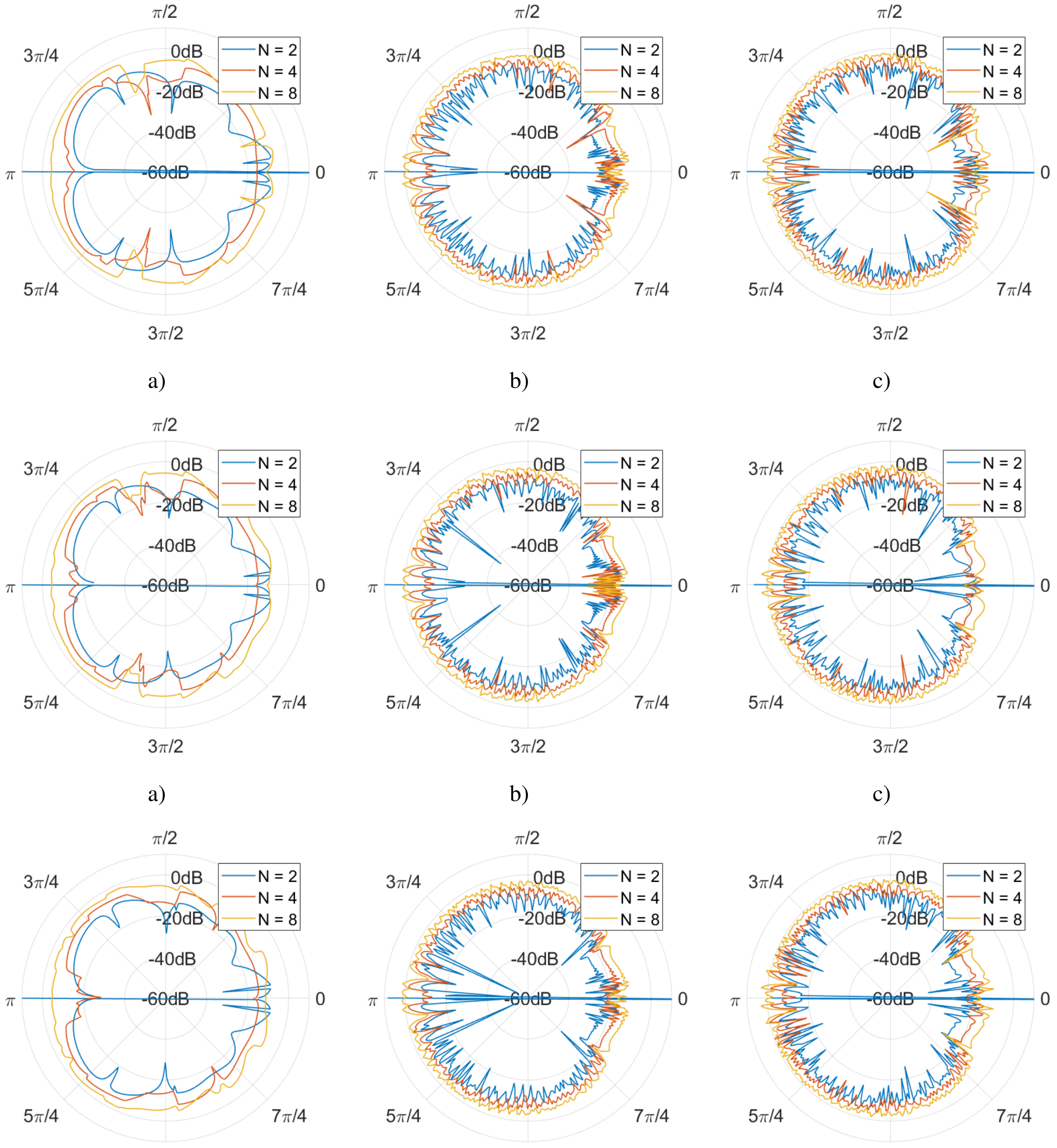

a) b) c)

a) b) c)

a) b) c)

Fig. 42: ΔG of the real gain as a function of the angle for an antenna located 20 cm away from the user model. The simulations for a plane wave of various frequencies are shown. The leftmost column represents the simulations obtained for an incident wave of 1GHz. The centre column does so for a 30GHz wave while the right one depicts the 60GHz wave. The first row uses a Type 1 cylinder (11 cm), the second a Type 2 cylinder (13.3 cm) and the third row a Type 3 one (16 cm). Each tile depicts the gain of the antenna for 2, 4 and 8 elements.

REFERENCES

[1] O. P. Gandhi and A. Riazi, "Absorption of Millimeter Waves by Human Beings and its Biological Implications," *IEEE Transactions on Microwave Theory and Techniques*, vol. 34, no. 2, pp. 228-235, Feb. 1986.

[2] T. Wu, T. S. Rappaport and C. M. Collins, "Safe for Generations to Come: Considerations of Safety for Millimeter Waves in Wireless Communications," *IEEE Microwave Magazine*, vol. 16, no. 2, pp. 65-84, Mar. 2015.

[3] T. Wu, T. S. Rappaport and C. M. Collins, "The Human Body and Millimiter-Wave Wireless Communications Systems: Interactions and Implications," *IEEE International Conference on Communications*, Jun. 2015.

[4] A. Alexiou, P. Kostarakis and V.N. Christofilakis, "Interaction Between GSM Handset Helical Antenna and User's Head: Theoretical Analysis and Experimental Results," *Environment Systems and Decisions*, vol. 25, pp. 215-221, 2005.

[5] D. G. Brennan, "Linear Diversity Combining Techniques," *Proceedings of the IEEE*, vol. 91, no. 2, pp. 331-356, Feb. 2003.

[6] X. Dong, N. C. Beaulieu, "Optimal Maximal Ratio Combining With Correlated Diversity Banches," *IEEE Communication Letters*, vol. 6, no. 1, pp. 22-24, Jan. 2002.

[7] B. Holter, G. E. Øien, "The Optimal Weights of a Maximal Ratio Combiner Using an Eigenfilter Approach," *Norwegian University of Science and Technology: Department of Telecommunications*

[8] G. Kevin Zhu (2020). Cylinder scattering (https://www.mathworks.com/matlabcentral/fileexchange/30162-cylinder-scattering), *MATLAB Central File Exchange*. Retrieved July 21, 2020

[9] R. F. Harrington, "Time-Harmonic Electromagnetic Fields" Piscataway, NJ: *IEEE Press*, 2001.

[10] F. Frezza, F. Mangini, and N. Tedeschi "Introduction to electromagnetic scattering: tutorial," *Journal of the Optical Society of America*, vol. 35, no. 1, pp. 163-173, Jan. 2018.

[11] C. A. Balanis, "Advanced Engineering Electromagnetic," New York, NY: *Jhon Wiley & Sons, Inc.*, 1989.

[12] W.J. Wiscombe "Improved Mie scattering algorithms," *Applied Optics*, vol. 19, no. 9, pp. 1505-1509, May. 1980.

[13] C. Gabriel, S. Gabriel and E. Corthout, "The dielectric properties of biological tissues: I. Literature survey," *Phys. Med. Biol.*, vol. 41, no. 11, pp. 2231-2249, 1996.

[14] S. Gabriel, R. W. Lau and C. Gabriel, "The dielectric properties of biological tissues: II. Measurements in the frequency range 10 Hz to 20 GHz," *Phys. Med. Biol.*, vol. 41, no. 11, pp. 2251-2269, 1996.

[15] S. Gabriel, R. W. Lau and C. Gabriel, "The dielectric properties of biological tissues: III. Literature survey," *Phys. Med. Biol.*, vol. 41, no. 11, pp. 2231-2249, 1996.

[16] I. Dove "Analysis of Radio PropagationInside the Human Body for in-Body Localization Purposes," *UNIVERSITY OF TWENTE: Faculty of Electrical Engineering, Mathematics & Computer Science*, Aug. 2014.

[17] C.W. Kim, and T.S.P See, "RF Transmission Power Loss Variation with Abdominal Tissues Thickness for Ingestible Soure," 13^{th} *International Conference on e-Health Networking, 2011.*, IEEE, Jun. 2011, pp.282-287.

[18] P. Arab, M. Heimlich, and E. Dutkiewicz, "Investigation of Radar Localization System Accuracy for Human Gastro Intestine (GI) Tract," 7^{th} *International Sympoisum on Medical Information and Communication Technology (ISMICT), 2013.*, IEEE, 2013, pp.144-148.

[19] S. K. Kim, H. J. Kim, K.Y. Hur, S.H. Choi, C.W. Ahn, S.K. Lim, K.R. Kim, H.C. Lee, K.B Huh, and B.S. Cha, "Visceral fat thickness measured by ultrasonography can estimate not only visceral obesity but alo risks of cardiovascular and metabolic diseases," *The American Journal of Clinical Nutrition*, vol. 79, no. 4, pp. 593-599, 2004.

[20] Y. Lee, and K. Hwang "Skin thickness of Korean adults," *Surgical and Radiological Anatomy*, vol. 24, pp. 183-189, Jul. 2002.

[21] H. Kanehisa, M. Miyatani, K. Azuma, S. Kuno, and T. Fukunaga "Skin thickness of Korean adults," *European Journal of Applied Physiology*, vol. 91, pp. 534-537, Jan. 2004.

[22] M. Zhadobov, N. Chahat, R. Sauleau, C. Le Quement and Y. Le Drean, "Millieter-wave interactions with the human body: state of knowledge and recent advances," *International Journal of Microwave and Wireless Technologies*, vol. 3, no. 2, pp. 237-247, 2011.

[23] Hasgall PA, Di Gennaro F, Baumgartner C, Neufeld E, Lloyd B, Gosselin MC, Payne D, Klingenböck A, Kuster N, "IT'IS Database for thermal and electromagnetic parameters of biological tissues," Version 4.0, May 15, 2018, DOI: 10.13099/VIP21000-04-0. itis.swiss/database

[24] R. George, J. Dela Cruz, R. Singh, O. Stuart *MRI Master,* London, United Kingdom, 2020. Accessed on: Nov. 14, 2020. [Online]. Available: https://mrimaster.com/anatomy%20abdomen%20axial.html

[25] V. Mishra, N. Kumar, S. Puthucheri, V. Agarwala, D. Singh, "Computation of Effective Dielectric Constant and Electric Field in the Human Head: A Preliminary Study for Electromagnetic Wave Effect," *International Conference on Industrial and Information Systems*, Sri Lanka, Dec. 2015.

[26] G.P. de Loor "Dielectric properties of heterogeneous mixtures containing water," $3^r d$ *Symposium on Microwave Power*, Boston, Mar. 1968.

[27] C. A. Balanis, "Antenna Theory. Analysis and Design," Hoboken, NJ: *Jhon Wiley & Sons, Inc.*, 2016.

[28] S.I, Alekseev and M.C. Ziskin, "Human Skin Permittiviy Determined by Millimeter Wave Reflection Measurements," *Bioelectromagnetics*, vol. 28, pp. 331-339, 2007.

[29] H. Hwang, J. Yim, J. Cho, C. Cheon and Y. Kwon, "110 GHz Broadband Measurement of Permittivity on Human Epidermis Using 1mm Coaxial Cable," *University of Seoul: Department of Electrical Engineering*, 2003.

[30] N. Chahat, M. Zhadobov, R. Augustine and R. Sauleau, "Human skin permittivity models for millimetre-wave range," *ELECTRONICS LETTERS*, vol. 47, no. 7, Mar. 2011.